Homogeneous CO_2 conversion by microwave plasma: wave propagation and diagnostics

N. den Harder,[1] D. C. M. van den Bekerom,[1] M. F. Graswinckel,[1] J. M. Palomares,[1] F. J. J. Peeters,[1] S. Ponduri,[1] T. Minea,[1] W. A. Bongers,[1] M. C. M. van de Sanden,[1,2] and G. J. van Rooij[1]

[1)] *FOM Institute DIFFER, Dutch Institute for Fundamental Energy Research, P.O. box 6336, 5600 HH Eindhoven, The Netherlands.*[a)]

[2)] *Department of Applied Physics, Plasma and Materials Processing Group, Eindhoven University of Technology, P.O. Box 513, 5600 MB Eindhoven, The Netherlands*

(Dated: 30 June 2016)

A suite of diagnostics is proposed to characterize microwave plasma dissociation of CO_2: laser scattering, Fourier Transform Infrared Spectroscopy, and spontaneous emission imaging. It provides a comprehensive performance characterization as is illustrated on the basis of experiments in a rudimentary 2.45 GHz, 1 kW microwave reactor. For example, two operating regimes are identified as function of pressure: the diffuse and constricted plasma mode. Their occurrence is explained by evaluation of microwave propagation, which changes with the electron-heavy particle collision frequency ν_{e-h}. In the diffuse mode, gas temperatures of 1500 - 3500 K are determined. The measured conversion degree, specific energy input, and temperature are summarized in a two-temperature thermal model, which is solved to obtain the gas temperature at the periphery of the reactor and the size of the hot zone. Solutions are found with edge temperatures of hundreds of K, and hot zone fractions which agree with the measured behaviour. The agreement shows that non-thermal processes play only a marginal role in the measured parameter space of the diffuse discharge. In the constricted mode, the radial plasma size is independent of power. A skin depth equal to the plasma size corresponds to electron densities of 10^{18} - 10^{19} m^{-3}. Temperatures in the central filament are in the range 3000 - 5000 K. Both discharge modes are up to 50 % energy efficient in CO production. Rayleigh signals increase in the afterglow, hinting at rapid gas cooling assuming that the gas composition remains unchanged.

[a)]Electronic mail: G.J.vanRooij@DIFFER.nl

I. INTRODUCTION

Anthropogenic emissions of greenhouse gases are at a historic high, and the associated changes in atmospheric composition have resulted in a global surface temperature increase[1]. Concerns about human-induced climate change have led to an increased use of renewable sources for energy generation. Most of these sources are intermittent, and fluctuations lead to periods where the supply exceeds the demand, during which time energy storage is needed. In addition, most renewable sources produce electricity, while less than 20 % of the total energy is consumed in that form[2]. Converting electrical energy into chemical fuels would thus not only be useful for energy storage, but also for sector integration: deployment of sustainable energy in e.g. transportation. In addition, fuels are a long-term storage solution which is easily transportable over global distances. The present paper considers the characterization of microwave plasma for the homogeneous reduction of CO_2 as a first step in such fuel production from renewable energy.

It might go without saying within the context of the present special issue on plasma conversion that microwave plasma carries several advantages to electrify chemical conversions compared to more traditional methods such as thermolysis and electrolysis[3,4]. Nevertheless, we briefly highlight some. Firstly, microwave reactors can be switched on and off on sub-second timescales, which makes it compatible to intermittently available sustainable energy sources such as wind and solar. Furthermore, no rare materials are involved so that the technique is scalable, even up to the volumes of the energy market. Power densities are high, which allows for compact plants in distributed production schemes. And last but not least: microwave technology is cheap in terms of euro/watt, which also relates to compatibility to sustainable energy sources as significant reactor downtimes are not immediately prohibitive from a cost perspective.

Another strong argument supporting the choice for microwave plasma for the purpose of driving chemical conversions is found in the promising energy efficiencies, exceeding 80 %, that have been demonstrated for CO_2 dissociation[5]. These record efficiencies could be reached by virtue of the non-thermal, i.e. non-equilibrium, nature of these plasma discharges: different degrees of freedom have different temperatures. Promoting overpopulation of high vibrational modes was identified to enhance rates for dissociation. In effect, the high energy efficiencies were realized since most of the energy invested in vibrational excitation directly

contributes to dissociation. To sustain non-equilibrium between the gas temperature and the vibrational temperature, it is vital that a large fraction of the discharge energy is transferred from the plasma electrons to the vibrational modes. For CO_2 this is calculated to be the case for an electron temperature range of approximately 1-2 eV[5]. A low gas temperature is in addition essential to prevent fast relaxation of the vibrational modes into translational excitation and to maintain the overpopulation. Gas temperature measurements are therefore a good indication for the degree of non-equilibrium that is attained.

The purpose of the present article is to propose as well as introduce an ensemble of diagnostics that is able to comprehensively characterize the performance of a (microwave) plasma discharge for homogeneous conversion as well as to give insight in the degree of non-equilibrium that is attained to support achieving the highest possible energy efficiencies. However, before going into the details of these diagnostics, we will outline some basic concepts of microwave propagation theory. It will show how the absorption characteristics can strongly influence the plasma parameters, and therewith the effective discharge volume, and will be useful to understand the later observations. Subsequently, we will introduce the microwave reactor and detail the interfacing of the various diagnostics to it. Focussing on the diagnostic approaches and their synergetic value, we have kept the reactor design as simple as possible, as a straight flow tube inserted through a microwave waveguide, allowing optimal diagnostic access. The suite of diagnostics consists of laser scattering (in particular Rayleigh scattering), Fourier Transform InfraRed absorption (FTIR) spectroscopy and imaging of the spontaneous emission. Spontaneous emission profiles are used to characterize the different modes of plasma operation in dependence of pressures and to a lesser degree of power. The laser scattering is used to determine neutral density profiles from the Rayleigh scattering signals. The local neutral density determines firstly the microwave propagation via the electron-heavy particle collision frequency. Moreover, combining the density information with the reactor pressure gives insight in the temperature in the reactor and therewith provides a measure of the degree of non-equilibrium in the reactor. Neutral density profiles are also available in the afterglow of the plasma to characterize quenching behaviour. Finally, the composition of the effluent is measured with FTIR spectroscopy. The comprehensiveness of the approach is illustrated by combining the measured conversion degree, specific energy input, and neutral gas temperature into a two-temperature thermal model, which is solved to obtain the gas temperature at the periphery of the reactor and

the size of the hot zone.

II. MICROWAVE PROPAGATION AND ABSORPTION

Understanding of microwave propagation and absorption is the starting point for understanding power deposition in the plasma reactor and thus the intrinsic plasma volume and electron density. It is well known that the electron density determines the plasma frequency below which oscillating electromagnetic fields are efficiently shielded by the response of the electrons. Such shielding occurs over a skin depth within which microwave power will still be absorbed. In case of inefficient shielding, the power absorption by the plasma may determine the penetration depth of the microwaves. And finally, collisions between electrons and neutral particles may hinder the response of the electrons to the external field and decrease the shielding efficacy at frequencies below the plasma frequency. The purpose of this section is to derive criteria for wave propagation in plasmas with and without collisions. Expressions will be found for the real and imaginary part of the refractive index, which are functions of the neutral density, and the electron temperature and density. The refractive indices are used to calculate reactor relevant parameters. For example, changes in absorption behaviour as function of the neutral density will be estimated, which will give insight into overall electron density and plasma size.

The refractive index is the square root of the relative permittivity ϵ_r. Propagation of electromagnetic waves requires that the refractive index is real, i.e. $\epsilon_r > 0$. In the absence of collisions, the relative permittivity for a wave of angular frequency ω is given by:

$$\epsilon_r = 1 - \frac{\omega_p^2}{\omega^2} = 1 - \frac{n_e e^2}{m_e \epsilon_0 \omega^2} \tag{1}$$

Here, ω_p is the plasma frequency, determined by the electron density n_e. The equation carries the well-known plasma property that electromagnetic waves with frequencies lower than the plasma frequency are shielded and cannot propagate. In case of 2.45 GHz microwave radiation, wave propagation is thus possible at densities below the critical density 7.5×10^{16} m^{-3}.

As said, electron-neutral collisions will hinder the response of the electrons to the oscillating field and thus deteriorate the effective shielding so that microwaves below the plasma

frequency may still penetrate. These collisions change the relative permittivity as:

$$\epsilon_r = 1 - i\frac{\sigma_\omega}{\epsilon_0 \omega} \tag{2}$$

Here, σ_ω is the conductivity that depends on the electron heavy particle collision frequency ν_{e-h}:

$$\sigma_\omega = \frac{n_e e^2}{m_e}\frac{1}{\nu_{e-h} + i\omega} = \frac{n_e e^2}{m_e}\frac{\nu_{e-h} - i\omega}{\omega^2 + \nu_{e-h}^2} \tag{3}$$

The real part of the conductivity expresses the Ohmic losses, the imaginary part the inductive behaviour of the plasma. The real part dominates in collisional plasmas driven by 2.45 GHz microwaves. Combining Equations 2 and 3 yields:

$$\epsilon_r = 1 - \frac{\omega_p^2\left(1 + i\frac{\nu_{e-h}}{\omega}\right)}{\omega^2 + \nu_{e-h}^2} \tag{4}$$

The collision frequency ν_{e-h} is the sum of an electron ion and an electron neutral term:

$$\nu_{e-h} = \nu_{e-i} + \nu_{e-n} = n_i K_{e-i} + n_n K_{e-n} \tag{5}$$

with n_i and n_n the ion and neutral densities, and K_{e-i} and K_{e-n} the rate coefficients for momentum transfer from electrons to ions and atoms, respectively. The rate for electron-ion collisions is taken from Mitchner and Kruger[6]:

$$K_{e-i} = \frac{4\sqrt{2\pi}}{3}\left(\frac{e^2}{4\pi\epsilon_0 m_e}\right)^2\left(\frac{m_e}{k_B T_e}\right)^{3/2}\ln\sqrt{1+\eta^2\Lambda^2} \tag{6}$$

Here, Λ is the Coulomb logarithm

$$\Lambda = \frac{3k_B T_e 4\pi\epsilon_0}{e^2}\sqrt{\frac{\epsilon_0 k_B T_e}{e^2 n_e^2}}, \tag{7}$$

η is a factor close to one ($\eta = 1$ is used in all the calculations), and T_e the electron temperature. The electron ion collision rate is applicable for singly ionized plasmas and does not depend on the ion species. It is calculated using the total electron scattering cross section taken from Itikawa[7], which is converted to a rate as:

$$K(T_e) = \int_0^\infty f(E, T_e)\sigma(E)\sqrt{\frac{2E}{m_e}}\,\mathrm{d}E \tag{8}$$

A Maxwell-Boltzmann distribution is assumed for the electron energy distribution function $f(E, T_e)$:

$$f(E, T_e) = 2\sqrt{\frac{E}{\pi}}\left(\frac{1}{k_B T_e}\right)^{3/2}\exp\left(-\frac{E}{k_B T_e}\right) \tag{9}$$

Because the electron scattering cross section stays within the same order of magnitude in the energy range energy 1-100 eV, the rate calculation is not sensitive to the assumption of a Boltzmann distribution. Rate coefficients for momentum transfer to the ions and neutrals are shown in Figure **??**.

At ionization degrees below 10^{-3} the $n_n K_{e-n}$ term is dominant in the collision frequency. Figure **??** shows ν_{e-h} as function of neutral density for various electron densities at an electron temperature of 1 eV to illustrate the contribution of both terms on the total collision frequency. At experimentally relevant neutral densities, the electron-ion term starts playing a role above electron densities of 10^{19} m^{-3}. Below this electron density the collision frequency is mainly determined by the electron-neutral term. Via the collision frequency, the neutral density determines the microwave propagation behaviour as will be shown by analysis of the refractive indices.

The complex refractive index is (for nonmagnetic media) related to the relative permittivity as[8]:

$$n = n_{Re} + i n_{Im} = \sqrt{\epsilon_r} \tag{10}$$

Separating the real and imaginary parts after squaring the refractive index yields an analytical solution for the refractive indices in terms of the relative permittivity:

$$n_{Re} = \sqrt{\frac{1}{2}\left(\epsilon_{Re} + \sqrt{\epsilon_{Re}^2 + \epsilon_{Im}^2}\right)} \tag{11}$$

$$n_{Im} = \sqrt{\frac{1}{2}\left(-\epsilon_{Re} + \sqrt{\epsilon_{Re}^2 + \epsilon_{Im}^2}\right)} \tag{12}$$

Finally substituting the real and imaginary part of the relative permittivity described in Equation 4 results in:

$$n_{Re} = \sqrt{\frac{1}{2}\left(1 - \frac{\omega_p^2}{\omega^2 + \nu_{e-h}^2} + \sqrt{\frac{\nu_{e-h}^2\omega^2 + (\omega^2 - \omega_p^2)^2}{\omega^2(\omega^2 + \nu_{e-h}^2)}}\right)} \tag{13}$$

$$n_{Im} = \sqrt{\frac{1}{2}\left(\frac{\omega_p^2}{\omega^2 + \nu_{e-h}^2} - 1 + \sqrt{\frac{\nu_{e-h}^2\omega^2 + (\omega^2 - \omega_p^2)^2}{\omega^2(\omega^2 + \nu_{e-h}^2)}}\right)} \tag{14}$$

The overall behaviour of the real and imaginary part of the refractive index as function of the electron and neutral density at a microwave frequency of 2.45 GHz are shown in Figure **??**. These values are calculated for an electron temperature of 1 eV; results for an electron temperature of 0.5 and 2.0 eV are very similar. It is seen that the real part of the refractive

index changes behavior around a neutral density of 2.3×10^{23} m^{-3} for electron densities above the critical electron density.

The real and imaginary part of the refractive index as function of the electron density are shown in Figure **??** by dashed and dotted lines, respectively. The reflectance is also included as solid lines. These were calculated for an electron temperature of 1 eV and pure CO_2 as neutral species. It is evident that a low neutral density gives also a low electron-neutral collision frequency. Therefore, low neutral density means that neutral collisions are not effective to hinder the shielding of the external field by the electrons and thus the real part of the refractive index goes to zero while the imaginary part increases steeply as the electron density grows above the critical density. This change in refractive indices results in an increase of the reflection coefficient. Thus, at low neutral densities, microwave propagation limits the electron density to the *critical* density and causes the existence of the so-called *diffuse regime* Fridman[9]. Having a fixed upper limit for the electron density requires the plasma *volume* to adjust to the microwave power. At high neutral densities, the neutral collisions do hinder the shielding of the oscillating field by the electrons and allow the plasma density to increase above the critical density.

Having established that the neutral density is the dominant factor for the collision frequency, it is instructive to investigate how it changes the refractive index. Figure **??** shows the real and imaginary part of the refractive index as function of CO_2 density for various electron densities. The refractive index has a non-zero value over the complete range of neutral densities provided that the electron density is below the critical electron density, i.e. microwave propagation is possible regardless of collision frequency. The region where the real part becomes zero, i.e. above the critical density, reflects shielding of the electromagnetic waves by the plasma. Here, propagation becomes again possible if the electrons are hindered to follow the field by collisions with neutrals and/or ions.

Absorption length scales are characterized by the skin depth, which is defined as the distance over which the wave amplitude reduces by a factor $\frac{1}{e}$. Since the wave vector is given by $k = \frac{\omega}{c} n$, and only the imaginary part of the wave vector results in absorption, the skin depth is given by:

$$\delta_{Skin} = \frac{c}{\omega} \frac{1}{n_{Im}} \tag{15}$$

The skin depth describes dissipative stopping, the incoming energy flux decays as given by

the Beer-Lambert-Bouguer law:

$$S(x) = S_0 \exp\left(-\frac{2x}{\delta_{Skin}}\right) \tag{16}$$

The factor of two accounts for the fact that the energy flux is related to the square of the field, and the skin depth relates to the wave amplitude. As shown in Figure **??**, the skin depth becomes on the order of millimeters as the electron density increases. This results in a plasma filament at higher electron densities, which is described by Fridman[9] as the so-called *contracted regime*. When the relative permittivity becomes negative, the electromagnetic waves are unable to propagate. Under these conditions, the waves are reflected over a typical length scale:

$$\delta_{Reflection} = \frac{c}{\omega\sqrt{|n_{Re}^2 - n_{Im}^2|}} \tag{17}$$

This length scale is not related to energy dissipation, but corresponds to reflection. Parameter scans of the skin depth and the reflection length are shown in Figure **??**. Note that the length scale for reflection only makes physical sense when the waves are reflected, which is roughly in the lower right quadrant of the figure.

The refractive indices are also used to estimate microwave reflection, under the assumption that a plane wave is incident on a flat interface, where there is a sharp transition in refractive index. These assumptions are not satisfied in the reactor, but it is useful to have a rough estimate of the microwave reflection when scanning parameters over several orders of magnitude. The reflection coefficient is calculated with the Fresnel equation, given by:

$$R = \frac{(n_{Re} - 1)^2 + n_{Im}^2}{(n_{Re} + 1)^2 + n_{Im}^2} \tag{18}$$

A parameter scan of the reflection coefficient is shown in Figure **??**. The length scale over which reflection takes place scales inversely to the reflection coefficient. Equation 18 and 16 can be combined to estimate the efficiency with which power is coupled into the plasma:

$$\eta_{\mathrm{MW}} = (1 - R)\exp\left(-\frac{2l}{\delta_{Skin}}\right) \tag{19}$$

where l is the typical plasma size. A scan of Equation 19 for a plasma size of 1 cm as function of the neutral and electron density is also shown in Figure **??**. The analysis in this section is applied to plasmas driven by 2.45 GHz microwaves. At this microwave frequency, low power sources are inexpensive and readily available, and the size of magnetrons and waveguides is ideally suited for small-scale applications. However, 915 MHz microwaves have a higher

electricity to microwave efficiency, and potentially provide more power per single magnetron. At microwave frequencies of 915 MHz the propagation behaviour is similar, however, the numbers are slightly different. The critical electron density is 1.0×10^{16} m^{-3}, and, at 1 eV, higher electron densities become possible at a neutral density of 8.5×10^{22} m^{-3}.

On basis of these calculations, we make the following quantitative and qualitative observations for 2.45 GHz microwave propagation in CO_2 plasmas. In the absence of electron-neutral collisions, there is an upper limit on the electron density: 7.5×10^{16} m^{-3}. Hence, electron densities in excess of this critical density can only be reached by virtue of the electron-neutral collisions. Sustaining plasmas with electron densities in excess of the critical density at low neutral density will be limited by reflection, even when electron-heavy particle collisions are taken into account. Calculating the electron-heavy particle collision frequency ν_{e-h} with the appropriate cross section for CO_2 shows that electron densities in excess of the critical density become accessible above neutral densities of 2.3×10^{23} m^{-3}. This density is valid in a range around an electron temperature of 1 eV since the refractive indices are only weakly dependent on electron temperature. Below this neutral density, there will be a diffuse plasma with an electron density below the critical density. Above this neutral density, electron densities in excess of the critical density are not limited by reflection. However, as the electron density increases, the skin depth, the length scale over which absorption takes place, decreases. Increasing neutral density softens this behaviour somewhat, but in general the plasma size will be limited as the electron density increases, resulting in a contracted plasma filament.

In conclusion, the neutral density, electron density, and the plasma size are linked as result of microwave propagation. The results outlined in this section can help exclude unphysical solutions of models which do not include these effects. It can also provide insights on limitations when scaling up the reactor. A reactor operating at 915 MHz will have a smaller operating window in terms of pressure in which the discharge is diffuse. In the contracted regime, increasing the microwave power will only lead to a marginally larger plasma volume because of skin effects. A larger reactor operating in this regime would thus need to increase the contact between gas and plasma, either by creating parallel reactors, or by influencing the gas flow in the reactor.

III. GAS FLOW DYNAMICS

An empirical finding is that tangential injection of the feed gas is required to stabilize the plasma in the center of the flow tube, in particular in the contracted discharge regime. Wondering to what extend the imposed flow pattern that herewith is induced remains conserved downstream, which is only the case if the flow is laminar, we estimate here the flow regime. In addition, for convenience in the later interpretation of the data, the residence time of particles in the plasma will be calculated.

The characteristic, dimensionless number that classifies the flow regime is the Reynolds number, which is defined as the ratio of inertial to viscous forces. At Reynolds numbers lower than 1000, the viscous forces are dominant, the flow will be laminar, and flow fields may be assumed to propagate. At Reynolds numbers above 4000, inertial forces are dominant, which gives rise to turbulent flow.

The mean velocity of gas in the tube is given by:

$$v_{mean} = \frac{\Phi}{\pi R_{tube}^2 n_0} \tag{20}$$

where Φ is the number of particles entering the tube per second, R_{tube} is the radius of the flow tube, and n_0 is the neutral density. Inserting this relation in the expression for the Reynolds number yields:

$$Re = \frac{\rho_g v 2R_{tube}}{\eta(p,T)} = \frac{2m_{\mathrm{CO_2}}\Phi}{\pi R_{tube}\eta(p,T)} \tag{21}$$

Where ρ_g is the gas density, v is the gas velocity, η is the dynamic viscosity of the gas (Pa s), and $\mathrm{m_{CO_2}}$ is the mass of a carbon dioxide molecule.

For a CO_2 flow of at most 10 slm which is above 300 K and flows with a uniform velocity in a tube with an inner diameter of 27 mm, the Reynolds number is always lower than 1000[10]. This means that the flow is laminar in the complete parameter range studied in the reactor, and that an applied flow pattern will not be broken up by turbulence.

Given that the flow is laminar, there is Poiseuille flow, with the associated parabolic radial variation in the axial flow velocity for a tube with circular cross section as:

$$v(r) = \frac{2v_{mean}}{R_{tube}^2}(R_{tube}^2 - r^2) \tag{22}$$

It is assumed that in the experiment, the radial component of the velocity, i.e. the vortex flow, is superimposed on this parabolic axial velocity profile. Knowing the mean velocity

and the length of the plasma volume defines the residence times. Figure **??** shows calculated residence times when the length of the active volume is equal to the small dimension of the WR340 waveguides used in the experiment: 43.2 mm.

IV. THERMOLYSIS OF CO_2 AND QUENCHING

A key performance indicator for processes that convert electricity to fuels is the energy efficiency. Plasma dissociation of carbon dioxide has been demonstrated to reach energy efficiencies of 80 % as result of the non-equilibrium nature of the plasma[5]. This is in contrast to an inherently lower energy efficiency limit of thermal decomposition of CO_2. In this section, we will calculate as a benchmark the equilibrium compositions at different temperatures and pressures, and infer the corresponding thermolysis efficiency limits. In addition, a 0-D chemical kinetics model will be constructed to be able to estimate the timescales that are involved to reach equilibrium, and thus the quenching rates needed to preserve the formed CO. In effect, the calculation of the exact energy efficiency limits for thermal dissociation in dependence of various different quenching scenarios will allow to assess the importance of non-thermal processes.

At this point it is worth mentioning that when *thermal* or *thermodynamic equilibrium* conversion is mentioned within the present paper, this only refers to the *heavy particles*. The plasma is not assumed to be thermal or in thermodynamic equilibrium as always electron temperatures will be much higher than gas temperatures.

Specialized computer programs are available to calculate the equilibrium composition of a given mixture as function of pressure and temperature. Here, the NASA Computer program CEA is used, which is described in References Gordon and McBride[11], McBride and Gordon[12]. The calculated equilibrium composition of a carbon dioxide mixture at 100 mbar is shown in Figure **??**. The composition slightly shifts to CO_2 at increased pressures. The calculation includes the following species: CO_2, CO, O_2, C, O, C_2, O_3. Species for which the mole fraction is below 10^{-3}, such as C, C_2, and O_3, are not shown in the graph. The efficiency limit is calculated as the number of CO molecules $n_{\mathrm{mol,CO}}$, multiplied with the formation enthalpy per molecule ΔH_{CO}, divided by the total enthalpy change of the mixture ΔH_{mix}:

$$\eta = \frac{n_{\mathrm{mol,CO}} \Delta H_{\mathrm{CO}}}{\Delta H_{\mathrm{mix}}} \tag{23}$$

A formation enthalpy ΔH_{CO} of 2.93 eV per molecule is used, which corresponds to the reaction $\mathrm{CO_2} \longrightarrow \mathrm{CO} + \frac{1}{2}\ \mathrm{O_2}$[13]. This calculation assumes ideal quenching of the mixture, which means that the CO content is preserved. The role of oxygen radicals is not taken into account. The ideal quenching efficiency is limited because only a fraction of the input energy is spent on the production of carbon monoxide. For example, as Figure **??** shows, when heating to 2000 K, less than 0.1 mole of CO is formed, while the total mixture is heated. As shown in Figure **??**, the ideal quenching efficiency is not sensitive to the temperature and pressure, there is a large region in parameter space where efficiencies around 50 % are attainable. This is a result of the weak pressure dependence of the equilibrium composition.

Since all the reactants and products remain mixed in the gas phase, and quenching will likely not be instantaneous, chemical (back-)reactions continue during cooling. Some of these reactions consume carbon monoxide, reducing the energy efficiency. The temporal behaviour of the mixture during temperature ramps is studied numerically with a 0-D chemical kinetics model. Temperature-dependent rate coefficients of dominant reactions between the four included species $\mathrm{CO_2}$, CO, $\mathrm{O_2}$, and O are used as input. Table I shows constants to calculate rate coefficients as:

$$k(T) = k_0 \exp\left(-\frac{E_a}{k_{\mathrm{B}} T}\right) \tag{24}$$

Reaction rates are calculated with the rate coefficients, e.g. the change in CO concentration resulting from reaction 1 is given by:

$$\frac{\mathrm{d}n_{\mathrm{CO},1}}{\mathrm{d}t} = k_1(T) n_{\mathrm{CO_2}} n_{\mathrm{CO_2}} \tag{25}$$

The total reaction rate for each reactant is the sum total of all the reactions. The temporal behaviour of an initial mixture is calculated by numerically integrating the differential equations over discrete time steps.

The outcome of the model depends critically on the input data, and the unknown uncertainties of the rate coefficients make an error estimate on the final answer difficult. As consistency check, the ratio between the forward and backward reaction rate coefficient are calculated using the principle of detailed balancing[14]. The equilibrium constant is related to the Gibbs free energy of a reaction as:

$$\kappa_{eq}(T) = \exp\left(-\frac{\Delta G(T)}{RT}\right) \tag{26}$$

The equilibrium constant only depends on thermodynamical data, which can be found in Chase Jr.[13]. It is also expressed in terms of a product of partial pressures of the reactants as:

$$\kappa_{eq}(T) = \left(\frac{p}{p^o}\right)^{\alpha_g} \prod_j^{\#_{reac}} \left(\frac{\bar{p}_j}{p}\right)^{\alpha_j} \tag{27}$$

Where $\bar{p}_j$ is the equilibrium pressure of component j. α_j is the stoichiometric coefficient of component j, which is negative for reactants and positive for products. α_g is the sum of the stoichiometric coefficients. The superscript ^{o} refers to standard conditions, which is at a pressure of 1000 mbar[15].

In equilibrium conditions, the forward and backward reaction rate will be the same, e.g. for reaction 1 and 9 in Table I:

$$\begin{gathered} \bar{n}_{\mathrm{CO_2}} \bar{n}_{\mathrm{CO_2}} k_1(T) = \bar{n}_{\mathrm{CO}} \bar{n}_{\mathrm{O}} \bar{n}_{\mathrm{CO_2}} k_9(T) \\ \left(\frac{\bar{p}_{\mathrm{CO_2}}}{p}\right)\left(\frac{\bar{p}_{\mathrm{CO_2}}}{p}\right)\left(\frac{p}{k_{\mathrm{B}}T}\right)^2 k_1(T) = \left(\frac{\bar{p}_{\mathrm{CO}}}{p}\right)\left(\frac{\bar{p}_{\mathrm{O}}}{p}\right)\left(\frac{\bar{p}_{\mathrm{CO_2}}}{p}\right)\left(\frac{p}{k_{\mathrm{B}}T}\right)^3 k_9(T) \end{gathered} \tag{28}$$

This equation is rewritten, multiplying both sides with the ratio between pressures to read:

$$\frac{\left(\frac{\bar{p}_{\mathrm{CO}}}{p}\right)\left(\frac{\bar{p}_{\mathrm{O}}}{p}\right)\left(\frac{\bar{p}_{\mathrm{CO_2}}}{p}\right)}{\left(\frac{\bar{p}_{\mathrm{CO_2}}}{p}\right)\left(\frac{\bar{p}_{\mathrm{CO_2}}}{p}\right)}\left(\frac{p}{p^o}\right) = \frac{\left(\frac{p}{k_{\mathrm{B}}T}\right)^2 k_1(T)}{\left(\frac{p}{k_{\mathrm{B}}T}\right)^3 k_9(T)}\left(\frac{p}{p^o}\right) \tag{29}$$

Recognizing this as the expression for the equilibrium constant given in Equation 27, the relation between forward and backward reaction rates is written universally as:

$$\kappa_{eq}(T) = \left(\frac{p}{k_{\mathrm{B}}T}\right)^{-\alpha_g}\left(\frac{p}{p^o}\right)^{\alpha_g}\frac{k_{\rightarrow}(T)}{k_{\leftarrow}(T)} \tag{30}$$

Although Equation 30 was derived on the assumption of thermal equilibrium between the components, the relation is also true for a system that is not in thermodynamic equilibrium. The only requirement is that the distribution of relative velocities of the colliding particles is Maxwellian at temperature T[14].

The prefactors k_0 of the last eight reaction rate coefficients in Table I are corrected using detailed balancing. An additional consistency check is found in the left panel of Figure **??**. It shows the CEA thermal equilibrium composition together with the composition reached after numerically integrating the system of differential equations for 2.5 milliseconds. Time steps of a nanosecond and CO_2 as initial composition are used in the calculation. Although there are minor discrepancies, the overall behaviour is well reproduced, giving confidence

that the set of rate coefficients adequately describes the behaviour of a thermal carbon dioxide mixture.

The effects of any arbitrary temperature evolution can be calculated with this system of differential equations. Two identical temperature profiles with a different cooling rate are shown in Figure **??** as example . After an instantaneous temperature increase, concentrations reach steady with a characteristic equilibration time. When the mixture slowly cools, all the formed CO reacts back to CO_2. Faster quenching rates will preserve more of the formed CO. The equilibration times and the CO loss fraction will be quantified on basis of scans in equilibrium temperature and quenching rate.

The equilibrium composition is reached after a characteristic time. This time constant decreases with increasing temperature, simply because the rate coefficients increase with temperature, as is shown in the left graph in Figure **??**. The equilibration time is calculated on basis of the CO concentration time derivative. Steady state is defined as a situation where the change in fractional pressure divided by the fractional pressure is less than 100 s^{-1}. The equilibration times are typically shorter than the residence times, which are on the order of hundreds of microseconds. It indicates that species distributions will reach steady state if the plasma is thermal, i.e. when non-equilibrium processes are not dominating.

Back-reactions during cooling lead to loss of CO. Only at low temperatures, these reactions are suppressed, indicating the need for rapid quenching. The right graph of Figure **??** shows the fractional loss of CO as function of linear cooling rate for three different initial temperatures. Here, the final temperature in the cooling ramp was set to 300 K. The model is not detailed enough to determine the effect of different final temperatures since species which play a role in the chemistry at lower temperatures, such as ozone, are not included. The fractional CO loss is sensitive to the initial temperature because it determines the composition of the cooling mixture. At higher temperatures, there are more oxygen radicals which react with CO to form carbon dioxide. Sufficiently high cooling rate can suppress most of the back reactions. Spatial effects are not included in these calculations. If the discharge would be inhomogeneous, where e.g. only a small fraction of the gas passes trough the plasma, back reactions could be quenched by the abundance of carbon dioxide compared to the reaction products. Figure **??** shows the efficiency for thermal CO production as function of temperature and linear cooling rates, which includes the fractional CO loss.

In summary, the thermal composition of a CO_2 mixture, and the energy efficiency of CO

production is calculated with a model based on thermodynamic quantities. A 0-D chemical kinetics model is constructed on basis of 16 reactions between 4 species to investigate the dynamics of a thermal CO_2 mixture. Equilibrium compositions are reached on timescales below tens of microseconds if the mixture has a temperature in excess of 3000 K. Thermal CO production has an intrinsic energy efficiency limit of around 55 % because excess energy is spent in heating the reactants. In practice, the efficiency will be lower due to reactions of carbon monoxide and oxygen radicals to form carbon dioxide while the mixture cools down to room temperature. Linear cooling rates on the order of 10^9 K s^{-1} inhibit back reactions, but the fractional CO loss depends critically on the initial composition of the cooling mixture. Still, when back reactions during cooling are taken into account, there are regions in parameters space where efficiencies in excess of 40 % are attainable.

V. EXPERIMENTAL

A. Plasma reactor

The plasma reactor uses 2.45 GHz microwaves that are generated with a 0.8 kW power supply. The microwaves are coupled to the reactant gas flowing in a 27 mm inner diameter quartz tube. The tube is inserted through the long side of a WR340 waveguide. A sliding short circuit is positioned at a quarter wavelength from the center of the quartz tube, so that the electric field at the plasma position is maximized. Note that the wavelength is the guide wavelength λ_g, which depends on the frequency and the mode of transmission. For the TE0 mode, the dominant mode in rectangular waveguides, the cutoff wavelength is twice the dimension of the long side of the waveguide. The guide wavelength is always longer than the wavelength in free space, and is calculated as:

$$\lambda_g = \frac{\lambda}{\sqrt{1 - \left(\frac{\lambda}{\lambda_{cut}}\right)^2}} \tag{31}$$

Having 2.45 GHz waves in a WR340 waveguide, with dimensions 86.36 × 43.18 mm, gives 174 mm for the guide wavelength. Therefore, the sliding short is positioned at 44 mm from the center of the quartz tube. There is a 20 mm diameter hole in the sliding short, to perform optical measurements in the microwave cavity. The 14 mm thickness of the sliding short ensures a negligible microwave leakage, which was confirmed experimentally. The

impedance of the plasma is matched with a three-stub tuner to establish efficient coupling of microwaves to the plasma. The reflected power never exceeded 1 percent of the input power in the experiments discussed in the present paper.

Gas is injected tangentially into the quartz tube to create a rotating flow pattern. The experiments were carried out at gas flow rates between 0.1 and 10 standard liters per minute. The reactor is pumped at adjustable pumping speed, resulting in pressures between 1 and 1000 mbar. The pressure is monitored with two different methods. For pressures up to 10 mbar, a PKR 260 Compact FullRange™Gauge is used, above this range the measurement is not linear. At pressures above 10 mbar, an ASG2-1000 Active Strain Gauge is used. This pressure measurement relies on the deflection of a metal diaphragm, and is therefore independent of gas type. The accuracy of this gauge is ± 0.2 % full scale, which gives a measurement error of 2 mbar. The temperature coefficient is 0.03 % full scale per K, which gives a 30 mbar deviation when the gauge heats up 100 K.

B. Rayleigh scattering

Scattering of light is potentially a non-intrusive way to study plasma parameters *in situ*. Lasers are an excellent light source to use in such a diagnostic setup since they provide spatially coherent, polarized light of high intensity. *Rayleigh* scattering is *elastic* (as opposed to Raman scattering) light scattering by *bound* (as opposed to Thomson scattering) electrons in atoms and molecules (and even of particulates that are of small size compared to the wavelength of the light)[17]. It is generally used to diagnose atomic or molecular *densities*. Also within the present work it is used to measure gas densities: to evaluate electron-neutral collisions in order to assess microwave propagation and, more importantly, to estimate the local neutral gas temperature (invoking the ideal gas law) to assess the importance of non-equilibrium processes. In view of the diagnostic emphasis within the present paper as well as the subtleties that are involved in the implementation and interpretation of Rayleigh scattering, we briefly summarize some theoretical aspects of the technique before detailing its implementation in the microwave plasma reactor.

1. *Rayleigh scattering theory in a nutshell*

Generally in light scattering, the scattered power P_{scat} is given by:

$$P_{scat} = P_i n_s \frac{\mathrm{d}\sigma_\mathrm{s}}{\mathrm{d}\Omega} \Delta\Omega L_{det} \tag{32}$$

where P_i is the incident power, n_s is the density of the scattering species, $\frac{\mathrm{d}\sigma_\mathrm{s}}{\mathrm{d}\Omega}$ is the differential scattering cross section for scattering mechanism s, $\Delta\Omega$ is the solid angle of the collection optics, and L_{det} is the length of the detection volume.

The total scattering cross section σ_R for Rayleigh scattering on spherically symmetric particles is given (in units of m^2 per particle) by:

$$\sigma_R = \frac{8}{3}\pi^3 \frac{\alpha_{SI}^2}{\epsilon_0^2} \frac{1}{\lambda_i^4} \tag{33}$$

where λ_i is the wavelength of the incoming light. Note the strong wavelength dependence to the inverse fourth power. α_{SI} is the polarizability of the scattering species, which has the SI units of F m^2. The polarizability is related to the refractive index n at heavy particle density n_h, which is an experimentally accessible quantity:

$$\alpha_{SI} = \frac{3\epsilon_0}{n_h} \left(\frac{n^2 - 1}{n^2 + 2} \right) \tag{34}$$

The total scattering cross section is not dependent on the scattering geometry. However, the incident light induces a dipole in the same direction as the incident field polarization, and this leads to a characteristic angular dependence of the intensity of the scattered field. These geometry effects are captured in the differential scattering cross section, which reads:

$$\frac{\mathrm{d}\sigma_\mathrm{R}}{\mathrm{d}\Omega} = \frac{\pi^2 \alpha_{SI}^2}{\epsilon_0^2 \lambda_i^4} \cdot (1 - \sin^2\theta \cos^2\phi) \tag{35}$$

The angle θ is the scattering angle, i.e. the angle between the incident light vector and the scattered light vector. The angle ϕ is the angle between the polarization of the incoming light and the plane defined by the incoming light vector and the scattered light vector. The term cross section is often used as shorthand for either the total scattering cross section, the differential scattering cross section, or the differential scattering cross section at perpendicular angles. These distinct cross sections are related as:

$$\sigma_R = \oint_{4\pi} \frac{\mathrm{d}\sigma_\mathrm{R}}{\mathrm{d}\Omega} \mathrm{d}\Omega = \int_0^{2\pi} \int_0^{\pi} \frac{\mathrm{d}\sigma_\mathrm{R}}{\mathrm{d}\Omega} \sin\theta \mathrm{d}\theta \mathrm{d}\phi = \frac{8\pi}{3} \frac{\mathrm{d}\sigma_{\mathrm{R},\theta=\phi=90^\circ}}{\mathrm{d}\Omega} \tag{36}$$

The previously described Rayleigh scattering theory only applies to spherically symmetric particles, and molecules are generally not spherical. Because of the spatial structure of molecules, the polarizability depends on the orientation with respect to the applied electric field. As a result, the polarizability is no longer a single number, but a tensor which contains the polarizabilities for different orientations. However, since the molecules are randomly oriented, all orientations are averaged. The polarizability tensor then reduces to two parameters which are invariant with respect to rotation: the mean polarizability a and the anisotropy γ. Literature values of these molecular properties are given for a selection of species in Table II. The Rayleigh differential scattering cross section is expressed in terms of these two quantities as:

$$\frac{\mathrm{d}\sigma_{\mathrm{R}}}{\mathrm{d}\Omega} = \frac{\pi^2 a^2}{\epsilon_0^2 \lambda_i^4} \left(1 + \frac{10}{45}\frac{\gamma^2}{a^2}\right) \cdot (1 - \sin^2\theta \cos^2\phi) \tag{37}$$

This expression is often rewritten in terms of ρ_0, which is defined as the ratio of horizontally-to-vertically polarized light scattered at 90° for unpolarized incident light. ρ_0 relates to a and γ as:

$$\rho_0 = \frac{6\gamma^2}{45a^2 + 7\gamma^2} \tag{38}$$

The differential scattering cross section then reads in terms of ρ_0:

$$\frac{\mathrm{d}\sigma_{\mathrm{R}}}{\mathrm{d}\Omega} = \frac{\pi^2 a^2}{\epsilon_0^2 \lambda_i^4} \left(\frac{6 + 3\rho_0}{6 - 7\rho_0}\right) \cdot (1 - \sin^2\theta \cos^2\phi) \tag{39}$$

The ratio $\frac{6+3\rho_0}{6-7\rho_0}$ is generally called the King correction factor. When the incident light is linearly polarized at a 90° angle with respect to the observation direction, and the light is collected under a 90° angle with respect to the propagation direction, the vertically polarized, horizontally polarized, and sum of the two components is expressed in terms of an effective Rayleigh differential scattering cross section as:

$$\begin{aligned} \frac{\mathrm{d}\sigma_{\mathrm{R-V}}}{\mathrm{d}\Omega} &= \frac{\mathrm{d}\sigma_{\mathrm{R}}}{\mathrm{d}\Omega}\left(\frac{2 - \rho_0}{2 + \rho_0}\right) \\ \frac{\mathrm{d}\sigma_{\mathrm{R-H}}}{\mathrm{d}\Omega} &= \frac{\mathrm{d}\sigma_{\mathrm{R}}}{\mathrm{d}\Omega}\left(\frac{\rho_0}{2 + \rho_0}\right) \\ \frac{\mathrm{d}\sigma_{\mathrm{R-Tot}}}{\mathrm{d}\Omega} &= \frac{\mathrm{d}\sigma_{\mathrm{R}}}{\mathrm{d}\Omega}\left(\frac{2}{2 + \rho_0}\right) \end{aligned} \tag{40}$$

where the subscript $\mathrm{R-V}$ indicates vertically polarized light and $\mathrm{R-H}$ indicates horizontally polarized light arriving at the detection system.

Literature Rayleigh scattering cross sections are listed in Table III for the species of interest. Note that Rayleigh scattering cross sections can be calculated from the polarizability. Literature values for molecules include the King correction factor, and as such take into account depolarization effects. The values still need to be multiplied by a factor $\frac{2}{2+\rho_0}$ in order to use these cross sections for the experimental geometry used within the present paper.

Rayleigh theory describes the scattering behaviour of small particulates with sizes smaller (at least one order of magnitude) than the wavelength of the incident light adequately as well. The polarizability for small spherical particulates is given by[24]:

$$\alpha_{SI} = 3\epsilon_0 V \left(\frac{n^2 - 1}{n^2 + 2} \right) \tag{41}$$

where V is the volume of the particulate, and n is the refractive index. The differential scattering cross section can thus be written:

$$\frac{\mathrm{d}\sigma_\mathrm{R}}{\mathrm{d}\Omega} = \frac{16\pi^4 r^6}{\lambda_i^4} \left(\frac{n^2 - 1}{n^2 + 2} \right)^2 \cdot (1 - \sin^2\theta \cos^2\phi) \tag{42}$$

where r is the radius of the scattering particulate. Since the cross section depends on the sixth power of the particulates radius, the observed signal is heavily biased towards larger particulates. To put this into perspective, a CO_2 discharge with 1 weight percent of carbon as 1nm graphite particulates[25] produces as much Rayleigh scattering from particulates as from CO_2 molecules. If the same amount of carbon is in 10 nm radius particulates, their Rayleigh scattering contribution is 3 orders of magnitude larger.

Thermal movement of the scattering species causes a Doppler broadening of the Rayleigh scattered light:

$$\Delta\lambda_{FWHM} = 4\sqrt{\ln 2}\sqrt{\frac{k_B T_h}{m_h c^2}}\lambda_i \tag{43}$$

This broadening is in the present situation negligible compared to instrument broadening due to the low thermal speed on account of the large mass of the heavy particles. For CO_2, it follows that the Doppler width at a temperature of 1 eV for incident light of 532 nm is only 0.009 nm.

Interpretation of Rayleigh scattering measurements is not straightforward in the present situation as the scattering cross section is different for the species that are to be expected in the discharge, i.e., CO, O_2, and O in addition to the parent CO_2 (see Table III). The lower cross section for the reaction products would cause underestimation of the species density, and thus overestimation of the gas temperature, at locations with high dissociation.

At first one might estimate that the error made here will not be significant. For example, assuming a specific energy input of 1 eV per molecule and 100 percent energy efficient in creating CO and O_2, the density would be underestimated by only 10 percent by assuming pure CO_2. However, this estimation is only valid when the conversion is homogeneous inside the reactor. If instead the conversion profile would be (strongly) peaked, the errors could become more than a factor of two (as will follow below).

The density (and temperature) data in the present paper were corrected for this effect by assuming a thermodynamic equilibrium species mix throughout the reactor and calculating an *effective* Rayleigh scattering cross section as function of temperature. It is noted that this causes still an overestimation of the temperature if local temperature gradients were too steep to maintain thermodynamic equilibrium (which requires rather some steepness in view of 10 μs equilibration time at 3500 K). On the other hand, temperatures are underestimated if conversion was to be intensified by non-equilibrium processes.

The strategy is as follows. In first instance, the density is determined as if it were pure CO_2, the n_{CO_2}-equivalent. The density of the actual mixture, n_{mix}, follows from:

$$n_{\mathrm{CO_2}} = n_{\mathrm{mix}} \left(\frac{\mathrm{d}\sigma_{\mathrm{mix}}}{\mathrm{d}\Omega} \right) \left(\frac{\mathrm{d}\sigma_{\mathrm{CO_2}}}{\mathrm{d}\Omega} \right)^{-1} = \frac{p}{k_{\mathrm{B}} T_{\mathrm{mix}}} \left(\frac{\mathrm{d}\sigma_{\mathrm{mix}}(T_{\mathrm{mix}})}{\mathrm{d}\Omega} \right) \left(\frac{\mathrm{d}\sigma_{\mathrm{CO_2}}}{\mathrm{d}\Omega} \right)^{-1} \tag{44}$$

The temperature dependence is written explicitly in the last term. Note that the contribution of the electrons and ions to the pressure is negligible since their densities are orders of magnitude lower than the neutral density. Assuming that pressure is known (measured), the right hand side is only a function of temperature. The equilibrium composition is used to calculate the effective Rayleigh scattering cross section by summing the product of the cross sections and mole fractions, as shown Figure **??**. Since the cross section decreases with temperature, there exists a unique solution to Equation 44. In the data analysis, the composition at 100 mbar is used, and depolarization properties of species other than CO_2 are not taken into account.

The depolarization properties of the mixture change slightly with composition. When the differently polarized components of the scattered light are measured separately, it would provide a consistency check of the adaptive cross section procedure. Since the CO_2 depolarizes the scattered light more than CO or O_2, the ratio of the H and V polarized light changes when the the composition of the mixture changes. The cross section for the different polarizations, calculated with Equation 40 using information from Table II, is shown in

Figure **??**.

2. Implementation of Rayleigh scattering

A Continuum Powerlite™DLS 8000 Nd:YAG laser is used as light source in the scattering setup. Frequency doubling yields 0.5 J per pulse at 532 nm. The 10 Hz laser has a shot-to-shot energy stability of 3.5 % (1.2 % RMS). The power drift is 5.0 %, which was measured during 8 hours with a ΔT of $\pm$ 3 °C. The timing jitter is 0.5 ns, which is small compared to the 5-7 ns pulse duration[26].

An anti-reflection coated UV fused silica window is used to couple the laser light into the reactor. Straylight from parasitic scattering of the laser light is suppressed by placing the entrance window 2 meters away from the detection volume, and installing baffles in the vacuum. A critical aperture of 6 mm diameter is installed 505 mm in front of the detection volume, and a subcritical aperture of 12 mm diameter is placed 100 mm before the detection volume. The laser light is dumped approximately 2 meters after the detection volume in a beam trap installed in vacuum.

The laser beam is focused at the detection volume by a lens with a 2.4 m focal length. Since the beam divergence is 0.45 mrad, this results in a 1.08 mm diameter beam at the focus. The Rayleigh length, the distance along the propagation direction from the beam waist to the place where the area of the cross section is doubled, is 288 mm.

Scattered light is collected at a 90° polarization and scattering angle by a 100 mm focal distance lens with a 51 mm diameter. The magnification of the collection optics results in an axial detection range of approximately 20 mm. The scattered light is transported with an array of 400 μm diameter fibers to a home-built, single-pass spectrometer in Littrow arrangement with a 0.3 m focal distance, 0.08 m diameter Littrow lens. A Jobin Ivon type 520-25-120 square grating is used which measures 11 x 11 cm^2, has a groove density of 1200 mm^{-1} and is optimized for first order diffraction. The grating efficiency is only about 20 % as shown in Figure **??**[27]. The grating angle of the spectrometer is calculated with Braggs law:

$$2 \sin \alpha = nk\lambda \tag{45}$$

where n is the diffraction order, α is the grating angle, k is the groove density and λ is the wavelength of the incident light. The grating angle α is 0.325 radians, which is used to

calculate the linear dispersion:

$$\frac{d\lambda}{dx} = \frac{1}{knL}\cos\alpha \tag{46}$$

where L is the focal length of the Littrow lens. The linear dispersion is 26 nm per cm at the surface of the image intensifier.

A third generation image intensifier of type EPM102G-04-22S made by KATOD is used to amplify the measured signal. The in-house constructed power supply for the image intensifier has a rise time of 9 ns at a load of 150 pF, when a 1000 V pulse is requested. In these conditions, the fall time is 8 ns. A Nikon 135mm f/2 DC and a Nikon AF-S 85mm f/1.8g lens are used to project the intensified spectrum with a magnification of 0.6 on the MANTA G-145B CCD camera. The pixel size of this camera is 6.45 μm, with a resolution of 1388 x 1038. The magnification of the lenses gives an effective pixel size of approximately 11 μm at the image intensifier. Combining this with the calculated linear dispersion of 26 nm per cm at the surface of the image intensifier results in a linear dispersion of 0.027 nm/pixel. The linear dispersion of the spectrometer is also calibrated using a series of spectral lamps, yielding 0.026 nm per pixel. The small discrepancy with respect to the calculated value is likely due to a small uncertainty in the magnification of the image intensifier screen projection onto the CCD. A slit width of 10 μm was chosen, which results in an instrument FWHM of 0.03 nm. Since the linear dispersion is measured at 0.026 nm/pixel, this is close to critical sampling (i.e. instrument FWHM is equal to the sampling interval). The spectrometer etendue is calculated at 0.64×10^{-8}.

The quantum efficiency of the Manta G-145B camera is shown in Figure **??**. The quantum efficiency is measured by the manufacturer, without protection glass or filters, and the actual value is approximately 10 percent lower. Although Sony does not publish full well capacities, the CCD in the Manta G-145B camera, the Sony ICX285 (type 2/3), is reported to have a full well capacity of 18000 photoelectrons based on dynamic range and signal to noise calculations[28]. Low signal-to-noise ratios in the case of weak signals require long integration times. However, since the intensifier-CCD combination is uncooled, dark current and its associated noise levels will also increase at long acquisition times.

Calibration and data analysis is straightforward for Rayleigh scattering. Individual fibers are binned in the acquired spectra. Each bin is fitted with a Gaussian function to determine the amount of signal. The calibration of the detection branch sensitivity and straylight level is obtained from pressure scans. Calibration spectra are acquired multiple times to measure

statistical errors. Error propagation yields the error in the density determination. Variation in calibrations measured before and after experiments are an indication of the systematical error introduced by e.g. alignment changes over the course of the day. In most cases, both calibrations are within 10 %. An example is shown in Figure **??**. Note that the exposure time is varied, with single laser pulses being acquired at the upper end of the pressure range, so the statistical errors are different for the different points. The throughput always decreases towards the end of the day. Straylight levels are on the order of a few times 10^{21} m^{-3} CO_2 density equivalent, i.e. a few times 10^{19} m^{-3} electron density equivalent.

3. Estimation of laser heating

A potential error in the Rayleigh scattering measurement is local gas heating by the focussed laser beam. In the experimental setup, 0.5 J pulses focused into a 1.1 mm diameter spot result in fluences of 5×10^5 J m^{-2}. In these conditions, the non-intrusiveness of the diagnostic needs to be verified. Analytical expressions for laser heating of an electron gas with electron-ion and electron-atom interactions were derived by Carbone *et al.*[29,30]. The critical laser fluence F_{crit} to achieve an electron heating of ΔT_e reads as follows:

$$F_{crit} = 6\pi^2 \frac{m_e \epsilon_0 c^3}{e^2} \frac{k_B \Delta T_e}{\nu_{e-h} \lambda_i^2} \tag{47}$$

where ν_{e-h} is the collision frequency of the electrons with heavy particles, which is given above in Equation 5. The heated electrons will transfer the energy via collisions. At an electron temperature of 1 eV the electron-CO_2 collision rate is 6.8×10^{-14} m^3 s^{-1}, which results in 68 collisions during the 10 nanosecond laser pulse at a neutral density of 10^{23} m^{-3}. This energy transfer is not taken into account in the derivation, so this expression provides the upper limit for laser heating of the electron gas. Since the neutral density is orders of magnitude larger than the electron density, it is assumed here that if the condition for electron heating is not exceeded, neutral heating by the laser is not of importance.

The critical laser fluence calculated for several experimental conditions is shown in Figure **??**. A 10 % increase in electron temperature is taken as maximum allowed temperature variation. The electron density is fixed at 10^{19} m^{-3} in all cases, but the results are not sensitive to this value since ν_{e-h} is dominated by electron-neutral collisions. The fluence reached when a 0.5 Joule pulse is focused to a spot with 1.08 mm diameter is shown in

black. The experimental fluence exceeds the threshold for a ΔT_e of 10 % when the neutral density is sufficiently high. Since the neutral density at 300 K and 100 mbar is 2.4×10^{24} m^{-3}, laser heating could play a role already at low pressures, provided that the neutral gas is room temperature.

Although the previous calculations illustrate that laser heating could play a role, experimentally the effects of laser heating were observed only at much higher fluences by Carbone at al.Carbone *et al.*[29]. To exclude perturbation of the gas or plasma by the laser in the current experiment, a scan was made of in the laser power. Measured intensities are normalized by the pressure to account for scatter in the experimental conditions. For neutral gas, the Rayleigh scattered light shows a linear response as function of the laser power, indicating that processes which show a clear threshold, e.g. breakdown, do not occur. In a 3 slm CO_2 plasma created at 120 mbar and 830 Watt power input, the response is also linear, as shown in Figure **??**. Although these measurements do not, a priori, exclude laser heating in the complete parameter range accessible, they do prove that laser heating is not important for pressures up to 120 mbar. As will be shown later, neutral densities measured in the plasma are lower than expected, in which case the critical fluence is much higher than the laser fluence.

C. Optical emission imaging

Optical emission of the plasma in the reactor is studied using a Manta G-146B camera. The quantum efficiency is shown in Figure **??**. The emission is focused with a 1 inch diameter 75 mm focal distance lens at a distance of 284 mm which subtends a solid angle of 6.3×10^{-3} steradian. The magnification results in a field of view of approximately 20 by 20 mm. A vignetting correction is applied using a homogeneous discharge.

D. FTIR

The effluent is led through a gas cell inside a Varian 670 FTIR spectrometer. Spectra are taken at a resolution of 0.09 cm^{-1} so that the individual rovibrational peaks are resolved. CO densities are deduced from a fit of the spectrum. In the fit procedure, a spectrum is calculated using molecular data from the HITEMP database, taking into account pressure broadening,

Doppler broadening, and instrument broadening[31]. Room temperature is assumed since the FTIR measurement cell is located a few meters away from the discharge.

$$CO_2 \longrightarrow (1-\alpha)CO_2 + \alpha CO + \frac{\alpha}{2}O_2 \tag{48}$$

The energy efficiency is calculated using the enthalpy ΔH of 2.93 eV per molecule, and the measured conversion degree α[13].

$$\eta = \frac{\alpha \Delta H \Phi e}{P_{in}} \tag{49}$$

Φ is the flow rate in molecules per second, and P_{in} is the input power in Watt.

VI. RESULTS

A. Operating regimes in microwave discharges

Visual inspection of the microwave during coarse scans of power and pressure reveals two distinctly different modes of plasma operation. At low pressures the plasma is diffuse: the plasma emission is relatively homogeneous over the radius of the quartz tube. At higher pressures, the plasma constricts and forms a filament in the middle of the reactor. The difference between the diffuse and contracted regime is illustrated by the two optical emission images shown in Figure **??**.

The two operating regimes are not gradually different, but separated by a sharp transition. This follows from the FWHM of a Gaussian fit to the radial emission profile that is shown as function of input power in Figure **??** for a fixed flow rate of 13 slm. Note that the emission FWHM, although line-integrated, represents the plasma size, since the width of a Gaussian function is invariant under an Abel transformation[32]. The radial extent of the plasma is in the contracted regime more or less independent of input power, while in the diffuse regime the plasma radius increases when the input power is increased. In addition to the pressure dependence, these measurements suggest there is a minimum input power for the plasma to constrict. The total emission intensity increases for both regimes with power input as shown in Figure **??**. Deviations from this trend are attributed to emission outside of the observation volume.

The existence of the two regimes is explained by the differences in microwave propagation at different electron-heavy particle collision frequency. At low pressures, the collision

frequency ν_{e-h} is not sufficiently high to enable electron densities above the critical electron density of 7.5×10^{16} m^{-3}. This results in a diffuse plasma, where the plasma volume adjusts to satisfy the power balance. At increased pressures, above CO_2 densities of approximately 2.3×10^{23} m^{-3}, the collision frequency is high enough to enable the formation of plasma with electron densities in excess of the critical electron density. As the electron density increases the skin depth becomes smaller, limiting the plasma size. The filament is stabilized in the middle of the reactor by the rotating flow pattern created by the tangential injection of the feed gas.

The results section is divided into separate parts which describe the measurements in the diffuse and the constricted regime. This choice is made because the diffuse and contracted regime behave differently in terms of plasma parameters such as the electron density. The homogeneity of the diffuse regime allows the estimation of bulk properties with a two-temperature model. In the constricted regime, the plasma sizes obtained from optical emission measurements are used to estimate electron densities via the skin depth.

B. Low pressure operation: diffuse regime

On-axis Rayleigh scattering measurements interpreted on basis of the CO_2 Rayleigh cross section yield low neutral densities, corresponding to temperatures of up to 1 eV. At these temperatures, the CO_2 is fully dissociated into C and O, and this dissociation degree is reached on timescales that are well below the residence time. Thus, interpreting the Rayleigh signal assuming pure carbon dioxide as scattering species is unrealistic in these conditions. It is possible to account for the local dissociation degree in the interpretation of the Rayleigh scattering measurements, as outlined in the previous section in Equation 44. All density and temperature values presented here are calculated on basis of the effective cross section of a thermodynamic equilibrium mixture unless explicitly stated otherwise.

Profiles of the neutral density in the microwave cavity show only minor axial variations, as illustrated in Figure **??**. The ratio of the on-axis and 5 mm off-axis density approaches 1 when the power increases, as illustrated in the right graph of Figure **??**. This shows that the discharge is homogeneous over a large fraction of the reactor radius in the diffuse regime.

An overview of all the on-axis laser scattering measurements in the diffuse plasma is shown in Figure **??**. Different flow rates are used for each pressure setting. The measured

densities still overlap when plotted as function of pressure and input power, which means that the gas temperature is independent of gas flow rate. Measured neutral densities in the center of the diffuse plasma are below a neutral density of 2.3×10^{23} m^{-3}, the density that was calculated in Section II as the threshold below which the electron density is limited to 7.5×10^{16} m^{-3} to allow wave penetration. Consequently, the plasma density is more or less fixed and the plasma volume will adjust to the input power. Although the calculation is based on pure CO_2 (i.e. the electron-heavys particle collision frequency for CO_2), the transition away from the diffuse regime with neutral density occurs approximately as predicted.

Since the neutral density varies between 5×10^{22} and 25×10^{22} m^{-3}, and mostly flows of 13 slm are used, the mean flow speed varies between 40 and 200 m/s. The plasma length is roughly equal to the width of the waveguide, i.e. 43.2 mm, which gives residence times ranging from 0.2 to 1 ms. Starting with pure CO_2, an equilibrium composition is reached on a microseconds timescale.

Conversion degree as well as energy efficiency as a function of microwave power are shown in Figure **??** for various pressures. The conversion scales linearly with the power, with a different slope at different pressures. The neutral densities are a function of only input power at fixed pressure, whereas the energy efficiencies also depend on the flow rate. As Figure **??** shows, this results in different energy efficiencies for the same specific energy input. Since the plasma parameters are similar, we attribute the different energy efficiencies to a residence time effect. Thermal compositions are reached at short timescales, more plasma time only increases losses.

The offset in the energy axis intercept results in a hyperbolic behaviour of the energy efficiency as function of input power. Energy efficiencies close to 50 percent are reached at 103 mbar and 1 eV specific energy input. At a flow of 13 slm, this corresponds to a conversion degree of almost 15 percent. The measured energy efficiencies are below the limit of 52 percent for a thermal mixture which quenches instantaneously. At a specific energy input of 1 eV per CO_2 molecule, the calculated thermal mixture is below 2000 K, with less than 2 percent conversion degree and 6 percent energy efficiency. This does not correspond with the measured values, which is an indication that a one-temperature calculation is an oversimplification.

To estimate if the measured conversion degree and specific energy input can be reproduced by a model which assumes a thermal composition, a two-temperature model is introduced. In

this simple model, the conversion degree α and the specific energy input E_{in} are parametrized by three variables: the fraction of particles in the hot zone β, and two temperatures:

$$\begin{aligned} \alpha &= (1-\beta)\alpha(T_{low}) + \beta\alpha(T_{high}) \\ E_{in} &= (1-\beta)E_{in}(T_{low}) + \beta E_{in}(T_{high}) \end{aligned} \tag{50}$$

Back-reactions during quenching of the mixture are not considered. The record energy efficiency measurements with a conversion degree of 15 % at 1 eV specific energy input are reproduced with this model if 17 % of the gas is 3250 K (a value that was arbitrarily chosen) and 83 % of the gas is 720 K. Since radially outwards the surface area per annulus is larger, and the colder gas is denser, this results in a hot zone diameter of 19 mm if the density increase due to dissociation is neglected. This illustrates that CO production, even for the most optimum energy efficiencies of 50 %, is reproduced on basis of a thermal two-temperature model. The hot zone diameter is compatible with experimental observations, and the temperature of the cold zone allows for some gas heating at the sides of the plasma.

In the reactor the temperature profile will be not be a step function, due to heat convection and conduction. The effect of smoother profiles was investigated numerically with symmetric temperature profiles constructed with two logistic sigmoid functions. This analysis shows that temperature profiles with a steepness below approximately 1 mm yield solutions for E_{in} and α with reasonable edge temperatures.

With the measured conversion degree α, the specific energy input E_{in}, and the on-axis temperature T_{high} deduced from Rayleigh scattering measurements as input, the two-temperature model was solved for the hot zone fraction β and the temperature of the low temperature reservoir T_{low}. Figure **??** shows the hot zone fraction for a variety of measurements with CO_2 flow rates ranging from 3 to 13 slm. Although the efficiency (i.e. CO production) depends on flow and pressure, the hot zone fraction scales well with the specific energy input. This is consistent with the optically measured plasma size, which increases with input power. The 100 mbar power scans where the efficiency is optimal still have an appreciable cold zone temperature of 470 K and above. In some 3 slm cases, unphysical solutions were found. In these conditions, a high specific energy input and a T_{high} between 2300 and 2900 K, still result in a low conversion. We attribute this to CO losses via back reactions, so that the conversion degree which is measured downstream is not representative for the CO production. Figure **??** shows gas temperatures in the reactor for various oper-

ating conditions. The power scan at 101 mbar falls in the temperature range where the CO production is maximum, i.e. where the highest efficiencies are attainable. At the lower end of the measured temperature range, the residence time exceeds the chemical equilibration time. At 2500 K, the equilibration time is 0.4 ms, but this rapidly increases to 1.6 ms at 2250 K, and 7 ms at 2000 K. Although this is not compatible with the assumption made in the Rayleigh data analysis that the composition is in thermal equilibrium, the effect is small since at low temperatures the effective cross section is close to the CO_2 cross section.

The measured gas temperatures and CO production rates are consistent with a thermal composition and a sufficiently peaked temperature profile. In order to reach high energy efficiencies, it is vital that produced CO does not react back to CO_2. Back reactions are suppressed by quick cooling. Mixing with colder CO_2 from the edge of the reactor is beneficial in this respect for two reasons, firstly it is a cooling mechanism, and secondly the CO is diluted so that oxygen radicals are less likely to react with the carbon monoxide. Cooling rates of at least a few times 10^8 K/s are needed to keep the fractional CO loss below 20 %. The cooling rate of the gas is estimated from downstream Rayleigh scattering measurements, in the afterglow of the plasma. The measured cooling rates, whilst invoking the adaptive effective Rayleigh scattering cross section method, range between 10^6 and 10^8 K/s, which is insufficient to prevent back reactions. Although the cooling rates are modest, the intensity of the Rayleigh scattering does increase in the afterglow, as shown in the right graph in Figure **??** for a constricted discharge. Due to the variation of the effective cross section in this temperature range, the signal variation only translates to a minor temperature variation. Further interpretation of these measurements is speculative without knowing the exact composition. So either the composition does not change and the signal increases because of cooling, or the signal increases due to inward diffusion of CO_2, which has a higher Rayleigh scattering cross section. In any case, the temperatures measured in the afterglow are still around 3000 K, so further quenching must take place farther downstream.

C. High pressure operation: contracted regime

As the pressure increases, there is a transition in plasma shape: the plasma contracts to a filament in the middle of the reactor. This is a result of the increased collision frequency ν_{e-h}, which enables microwave propagation at electron densities above the critical density.

Because of the high power density in the small volume of the filament, the electron densities are estimated to be on the order of 10^{18} - 10^{19} m^{-3} with a simple power balance[33]. Indirect support for this electron density estimation is deduced from the plasma size. Since microwave propagation is limited by the skin effect, which changes with the electron density, the electron density is related to the plasma size. The radial extent of the plasma is on the order of millimeters, which corresponds to an electron density in the range 10^{18} - 10^{19} m^{-3} as calculated with Equation 15 (as the actual electron density profile will be somehow peaked, it is not justified to give any larger precision here). The filament is stabilized in the center of the reactor by the rotating flow pattern realized by axial injection of the carbon dioxide.

Axial profiles of the neutral density are measured with laser scattering for different radial locations. The left graph of Figure **??** shows profiles measured in similar discharges. As in the diffuse discharge, there are only minor variations in the axial direction. In the radial direction, there are large differences between the low neutral density in the plasma filament and the larger densities in the periphery.

A summary of the on-axis neutral density measurements is shown in Figure **??**. The measured densities and temperatures are shown as function of specific energy input since the measured values do not overlap when plotted as function of input power, but the paucity of measurements does not allow further conclusions. The neutral temperatures in the filament are higher than measured in the diffuse discharge, but not by a large margin. The measured on-axis neutral densities all exceed the the calculated n_0 of 2.3×10^{23} m^{-3} needed to sustain the constricted discharge mode. The energy efficiencies for the constricted regime are shown in Figure **??**. The maximum energy efficiency in the constricted regime is close to 50 percent, similar to values obtained in the diffuse regime. In contrast to operation at lower pressures, the energy efficiency scales with the specific energy input.

In the contracted plasma regime, the optical emission is peaked in the center of the reactor. This is a consequence of the peaked power deposition profile. The deposited power is transferred to the periphery by conduction. This situation is similar to electric arc discharges, although arcs generally operate at higher heavy particle temperatures. The behaviour of electrical arc discharges is described by the Elenbaas-Heller equation, which has analytical solutions[34]. The gas temperature profiles that result from the Elenbaas-Heller equation are not as peaked as the optical measurements suggest, these gradual profiles are not a good starting point for a two temperature approximation. Since the measured efficien-

cies in the contracted regime most likely result from a complex interplay of plasma-chemical processes, more measurements of the plasma parameters are needed for a factual discussion on the importance of non-equilibrium, vibrationally excited processes, in the contracted discharge.

VII. CONCLUSIONS

A suite of diagnostics has been proposed to characterize a microwave plasma reactor for the homogeneous dissociation of carbon dioxide. It consists of laser (Rayleigh) scattering, FTIR, and optical emission measurements, which is demonstrated to comprehensively characterize and explain conversion performance. Two regimes of operation are identified: a diffuse mode of operation at low pressures, and a constricted discharge at increased pressures. Their occurrence is caused by differences in microwave propagation. At low pressures, the collision frequency ν_{e-h} is not sufficiently high to enable electron densities above a critical electron density of 7.5×10^{16} m^{-3}. In this regime the plasma volume adjusts to satisfy the power balance. At increased pressures, above CO_2 densities of approximately 2.3×10^{23} m^{-3}, the collision frequency is high enough to allow electron densities in excess of the critical electron density. The increasing electron density makes the skin depth, over which microwave absorption occurs, smaller and hence limits the plasma size.

The neutral density is in the diffuse regime constant along the axial direction. The peaking observed in radial direction vanishes at a radius of 5 mm (presently the radial limit for the Rayleigh scattering) as the input power reaches its maximum of 800 W. The radial plasma size, estimated from optical emission measurements, increases with the input power, in accordance with the interpretation of the plasma volume adjusting to the power. Central gas temperatures in the range 1500 - 3500 K are inferred from Rayleigh scattering measurements. A two-temperature thermal model is constructed to relate the conversion degree α, the specific energy input E_{in}, a hot zone fraction β, and a T_{low} and T_{high}. Measured conversion degrees and specific energy inputs are combined with temperatures inferred from Rayleigh scattering measurements to obtain solutions for T_{low} and β. The hot zone fractions β scale with the specific energy input. The highest observed efficiencies are 50 % and are explained by thermal decomposition in the center with an edge temperature T_{low} of 470 K.

In the constricted regime, a small plasma filament forms in the middle of the reactor.

The radial size of the filament does not increase with increasing input power. The electron density is estimated to be in the range 10^{18} - 10^{19} m^{-3} based on the size of the plasma in combination with the calculated skin depth. Also in this regime, energy efficiencies approach 50 %.

Although the overall performance in terms of conversion and energy efficiency can fully be explained by thermodynamic equilibrium conversion of the neutral heavy particle population, it can not be excluded that non equilibrium process are still of importance in the plasma region. On the contrary, the present estimates for the quenching rates indicate that back reactions in the post plasma regions have been significant. In situ FTIR measurements revealing species distributions in the active plasma region and/or actively enhancing the cooling rate could resolve this present uncertainty.

REFERENCES

[1]IPCC, *Fifth Assessment Report: Climate Change 2014: The AR5 Synthesis Report* (Geneva: IPCC, 2014).

[2]IEA, *Key World Energy Statistics 2012* (International Energy Agency, 2012).

[3]H. Huang and L. Tang, Energy Conversion and Management **48**, 1331 (2007).

[4]E. Gomez, D. A. Rani, C. R. Cheeseman, D. Deegan, M. Wise, and A. R. Boccaccini, Journal of Hazardous Materials **161**, 614 (2009).

[5]V. D. Rusanov, A. A. Fridman, and G. V. Sholin, Soviet Physics Uspekhi **24**, 447 (1981).

[6]M. Mitchner and C. H. Kruger, *Partially Ionized Gases*, Wiley series in plasma physics (Wiley, 1973).

[7]Y. Itikawa, Journal of Physical and Chemical Reference Data **31**, 749 (2002).

[8]M. Leins, *Development and Spectroscopic Investigation of a Microwave Plasma Source for the Decomposition of Waste Gases*, Ph.D. thesis, Universität Stuttgart (2010).

[9]A. Fridman, *Plasma Chemistry* (Cambridge University Press, 2008).

[10]A. Fenghour, W. A. Wakeham, and V. Vesovic, Journal of Physical and Chemical Reference Data **27**, 31 (1998).

[11]S. Gordon and B. J. McBride, NASA Reference Publication 1311 (1994).

[12]B. J. McBride and S. Gordon, NASA Reference Publication 1311 (1996).

[13]M. W. Chase Jr., Journal of Physical and Chemical Reference Data Monograph 9 , 1

(1998).

[14]M. A. Lieberman and A. J. Lichtenberg, *Principles of Plasma Discharges and Materials Processing* (John Wiley & Sons, Inc., 2005).

[15]A. D. Mcnaught and A. Wilkinson, *IUPAC. Compendium of Chemical Terminology, 2nd ed. (the "Gold Book").* (WileyBlackwell; 2nd Revised edition edition, 1997).

[16]Y. P. Butylkin, A. A. Grinenko, A. A. Levitskii, L. S. Polak, N. M. Rytova, and D. I. Slovetskii, High energy chemistry **13**, 456 (1979).

[17]L. Rayleigh, Philosophical Magazine Series 5 **47**, 375 (1899).

[18]M. P. Bogaard, A. D. Buckingham, R. K. Pierens, and A. H. White, Journal of the Chemical Society Faraday Transactions 1 **74**, 3008 (1978).

[19]C. M. Penney, R. L. S. Peters, and M. Lapp, Journal of the Optical Society of America **64**, 712 (1974).

[20]T. N. Olney, N. M. Cann, G. Cooper, and C. E. Brion, Chemical Physics **223**, 59 (1997).

[21]A. K. Das and A. J. Thakkar, Journal of Physics B: Atomic, Molecular and Optical Physics **31**, 2215 (1998).

[22]M. Sneep and W. Ubachs, Journal of Quantitative Spectroscopy and Radiative Transfer **92**, 293 (2005).

[23]J. A. Sutton and J. F. Driscoll, Optics Letters **29**, 2620 (2004).

[24]A. R. Jones, Progress in Energy and Combustion Science **5**, 73 (1979).

[25]B. Stagg and T. Charalampopoulos, Combustion and Flame **94**, 381 (1993).

[26]Continuum, "Powerlite DLS 8000 Specifications," http://www.continuumlasers.com/files/products/powe (2015), [Online; accessed 23rd September 2015].

[27]Horiba, "Spectral efficiency curve," http://www.horiba.com/fileadmin/uploads/Scientific/Documents/Gr curve-520-25.pdf (2015), [Online; accessed 17th September 2015].

[28]A. Hornberg, *Handbook of Machine Vision*, 1st ed. (Wiley-VCH, 2006).

[29]E. A. D. Carbone, J. M. Palomares, S. Hübner, E. Iordanova, and J. J. A. M. van der Mullen, Journal of Instrumentation **7**, C01016 (2012).

[30]E. A. D. Carbone, J. M. Palomares, S. Hübner, E. Iordanova, and J. J. A. M. van der Mullen, Journal of Instrumentation **8**, E05001 (2013).

[31]L. S. Rothman, I. E. Gordon, R. J. Barber, H. Dothe, R. R. Gamache, A. Goldman, V. I. Perevalov, S. A. Tashkun, and J. Tennyson, Journal of Quantitative Spectroscopy and Radiative Transfer **111**, 2139 (2010).

[32]N. H. Abel, Journal für die reine und angewandte Mathematik **1**, 153 (1826).

[33]G. J. van Rooij, D. C. M. van den Bekerom, N. den Harder, T. Minea, G. Berden, W. A. Bongers, R. A. H. Engeln, M. F. Graswinckel, E. Zoethout, and M. C. M. van de Sanden, Faraday Discussions **183**, 233 (2015).

[34]B. D. Shaw, Journal of Applied Physics **99**, 034906 (2006), 10.1063/1.2168026.

TABLES

Index	Reaction	k_0	E_a (eV)
1	$CO_2 + CO_2 \longrightarrow CO + O + CO_2$	4.38×10^{-10}	5.58
2	$CO_2 + CO \longrightarrow CO + O + CO$	4.38×10^{-10}	5.58
3	$CO_2 + O_2 \longrightarrow CO + O + O_2$	3.72×10^{-13}	5.19
4	$CO_2 + O \longrightarrow CO + O_2$	7.77×10^{-15}	1.57
5	$O_2 + O_2 \longrightarrow O + O + O_2$	8.14×10^{-12}	5.14
6	$O_2 + O \longrightarrow O + O + O$	1.99×10^{-11}	4.98
7	$O_2 + CO \longrightarrow O + O + CO$	2.41×10^{-12}	5.12
8	$O_2 + CO_2 \longrightarrow O + O + CO_2$	2.57×10^{-12}	5.14
9	$CO + O + CO_2 \longrightarrow CO_2 + CO_2$	6.54×10^{-42}	0.13
10	$CO + O + CO \longrightarrow CO_2 + CO$	6.54×10^{-42}	0.13
11	$CO + O + O_2 \longrightarrow CO_2 + O_2$	6.51×10^{-45}	0.13
12	$CO + O_2 \longrightarrow CO_2 + O$	1.23×10^{-15}	1.32
13	$O + O + O_2 \longrightarrow O_2 + O_2$	6.81×10^{-43}	0.00
14	$O + O + O \longrightarrow O_2 + O$	2.19×10^{-42}	-0.20
15	$O + O + CO \longrightarrow O_2 + CO$	2.76×10^{-43}	0.00
16	$O + O + CO_2 \longrightarrow O_2 + CO_2$	2.76×10^{-43}	0.00

TABLE I: Rate coefficients of reactions between CO_2, CO, O_2, and O. k_0 is given in $m^3\ s^{-1}$ for bimolecular, and $m^6\ s^{-1}$ for termolecular reactions. The first and last eight reactions are each others inverse[16].

Species	α **(10^{-40} Fm^2)**	γ **(10^{-40} Fm^2)**	ρ_0 **(Percent)**	**Reference**
CO	2.22	0.62	1.0	[18]
CO_2	2.95	2.38	7.8	[18]
O_2	1.74*	1.27	6.6	[19]

TABLE II: Polarizabilities, polarizability anisotropies, and depolarization ratios for selected molecules at an incident wavelength of 532 nm. * For oxygen the static dipole polarizability is listed[20].

Species	$\frac{d\sigma_R}{d\Omega}$ **(10^{-32} m^2)**	**Reference**
C	5.8	[21]
CO	7.39	[22]
CO_2	14.8	[22]
O	1.2	[21]
O_2	5.13	[23]

TABLE III: Rayleigh scattering cross sections at 532 nm, 295 K, and $\theta = \phi = 90°$.

FIGURE CAPTIONS

FIG. 1. Rate coefficients for momentum transfer from electrons to ions and CO_2 atoms. K_{e-i} is calculated using Equation 6, at an electron density of 10^{19} m^{-3}. K_{e-n} is calculated from the Itikawa[7] cross sections using Equation 8.

FIG. 2. The collision frequency between the electrons and heavy particles as function of CO_2 density for various electron densities. At experimentally relevant neutral densities, electron-ion collisions only start playing a significant role above electron densities of 10^{19} m^{-3}.

FIG. 3. The real and imaginary part of the refractive index as function of the CO_2 and electron density. The real part of the refractive index shows different behaviour below and above a neutral density of 2.3×10^{23} m^{-3} for electron densities below and above the critical electron density of 7.5×10^{16} m^{-3}.

FIG. 4. Left: the real (dashed lines) and imaginary (dotted lines) part of the refractive index as function of electron density at various neutral densities. The reflection coefficient is indicated with solid lines. At low neutral densities, the reflection jumps to 1 above the critical density. When the collision frequency ν_{e-h} increases, the criteria for propagation are relaxed. Right: The real (solid lines) and imaginary (dashed lines) part of the refractive index as function of the neutral density for various electron densities. The green line marks the neutral density at which the collision frequency ν_{e-h} equals the microwave frequency ω in the absence of e-i collisions.

FIG. 5. Calculated skin depths as function of the electron density for various neutral densities. Using this graph the electron density can be estimated for a given neutral density with a measurement of the plasma size.

FIG. 6. Length scales of absorption and reflection as function of the electron and neutral density.

FIG. 7. Reflection coefficient (left) and absorption fraction (right) as function of the electron and neutral density for a 1D plasma of 1 cm wide.

FIG. 8. Calculated residence times for a reactor with a 27 mm inner diameter quartz tube and an active volume of 43.2 mm length.

FIG. 9. The equilibrium composition of a carbon dioxide mixture as function of temperature at a pressure of 100 mbar[11,12].

FIG. 10. Calculated gas composition and temperature as function of the specific energy input at a pressure of 100 mbar.

FIG. 11. The efficiency in case of ideal quenching as function of temperature and pressure. There is a large region in parameter space where efficiencies around 50 % are attainable.

FIG. 12. Left: comparison of the CEA code (lines) and the 0-D model based on the rate coefficients (dots). The overall behaviour of the system of equations matches the CEA equilibrium calculation. Right: Two temperature evolutions with cooling rates of 10^8 and 10^9 K/s (dashed and solid lines). Two different temperature evolutions are included to illustrate that the composition changes as the CO_2 mixture heats and cools.

FIG. 13. Left: CO equilibration time as function of equilibrium temperature. A CO_2 mixture reaches chemical equilibrium on a microseconds timescale, thus, high cooling rates are needed to suppress CO loss. Right: CO loss fractions as a function of the cooling rate. The increasing O radical concentration with temperature leads to a larger fractional CO loss.

FIG. 14. The efficiency of thermal CO production in the case of linear cooling rates. Sufficiently high cooling rates on the order of 10^9 K s^{-1} inhibit back reactions, and energy efficiencies in excess of 40 % are reached.

FIG. 15. The microwave setup consists of a magnetron (1) and a three port circulator with a matched, actively cooled load (2) which serves to shield the source from reflected

microwaves. A sliding short (5) and a three-stub tuner (3) maximize the electric field at the location of the plasma in the quartz tube (4).

FIG. 16. The equilibrium composition is used to calculated an effective cross section. The dashed lines indicate the cross sections for individual species.

FIG. 17. The equilibrium composition is used to calculated an effective cross section for the different polarization components. The ratio of the two components changes with temperature because of the different depolarization properties of the scattering species.

FIG. 18. A schematic of the spectrometer. Light enters via the slit (1), is reflected by a mirror (2) passes through the Littrow lens (3), refracts on the grating (4), passes the Littrow lens again, is amplified by the image intensifier (5), which is projected by lenses (6,7) onto the CCD (8).

FIG. 19. Efficiencies of components in the Solar Fuels spectrometer taken from the manufacturer specifications.

FIG. 20. Before and after experiments the signal intensity is measured as function of pressure to calibrate the sensitivity of the detection branch. Red points were measured during experiments. Similar throughputs over the course of the day indicate that the alignment of the optical system is stable. Intensity variations are used to calculate the statistical errors.

FIG. 21. Critical laser fluences for an electron heating of 10 %. An electron density of 10^{19} m^{-3} is used, but the results are not sensitive to this value since the ν_{e-h} is dominated by electron-neutral collisions. The fluence reached in the experiment is indicated in black.

FIG. 22. Laser power scans in 120 mbar CO_2 (left) and in a 3 slm CO_2 plasma at 120 mbar and 830 Watt power input (right). To eliminate scatter, the intensities are normalized to the pressure.

FIG. 23. Two optical emission measurements that illustrate the difference between the diffuse and contracted operating regime. Left: diffuse emission at a pressure of 42 mbar and

221 Watt input power. Right: contracted emission at a pressure of 170 mbar and 420 Watt input power.

FIG. 24. The FWHM and total intensity of the optical emission of the plasma. Left: the FWHM of the radial emission profile increases with power below approximately 130 mbar. Above this pressure the plasma width constricts to a few mm, and becomes independent of the microwave power. Right: The emission intensity increases linearly with power. At higher pressures, the emission is more intense. Deviations from the trend at higher power input is due to emission outside the detection volume.

FIG. 25. Axial profiles of the neutral density measured at different radii show minor variations. In the diffuse regime, the plasma becomes radially homogeneous as the input power increases.

FIG. 26. The neutral density in the center of the discharge for various pressures. Different flow rates were used at pressures of 39 mbar and higher.

FIG. 27. Left: conversion degree as function of microwave power for various pressures at an input flow of 13 slm. Right: Energy efficiencies as function of specific energy input at a reactor pressure of 103 mbar. At low flow rates, the energy efficiency becomes lower, this is attributed to increased losses for longer residence times.

FIG. 28. Hot zone fraction as function of the specific energy input for diffuse discharges, using the two-temperature model with the measured central temperatures and conversion degrees.

FIG. 29. The gas temperature in the center of the discharge calculated with the neutral density and reactor pressure.

FIG. 30. Axial profiles of the neutral density in the microwave cavity and afterglow of the plasma for contracted discharges. Left: in the contracted regime, there are pronounced radial gradients in the neutral density profiles, a consequence of the peaked power deposition

profile. Right: The CO_2 equivalent density increases in the afterglow, but the temperature decrease is modest as result of the temperature dependent cross section used in the analysis.

FIG. 31. On axis neutral densities (left) and temperatures (right) are interpreted assuming a thermal mixture as as calculated in Figure **??**.

FIG. 32. The conversion degree (left) and energy efficiency (right) as a function of the specific energy input in the constricted regime.

FIGURES

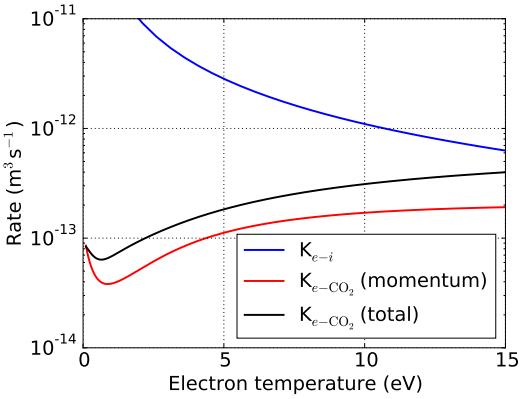

FIG. 1: Rate coefficients for momentum transfer from electrons to ions and CO_2 atoms. K_{e-i} is calculated using Equation 6, at an electron density of 10^{19} m^{-3}. K_{e-n} is calculated from the Itikawa[7] cross sections using Equation 8.

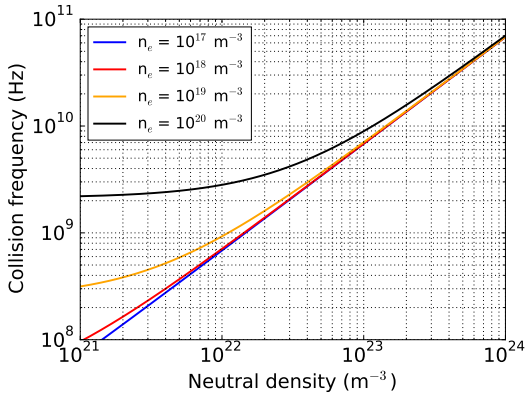

FIG. 2: The collision frequency between the electrons and heavy particles as function of CO_2 density for various electron densities. At experimentally relevant neutral densities, electron-ion collisions only start playing a significant role above electron densities of 10^{19} m^{-3}.

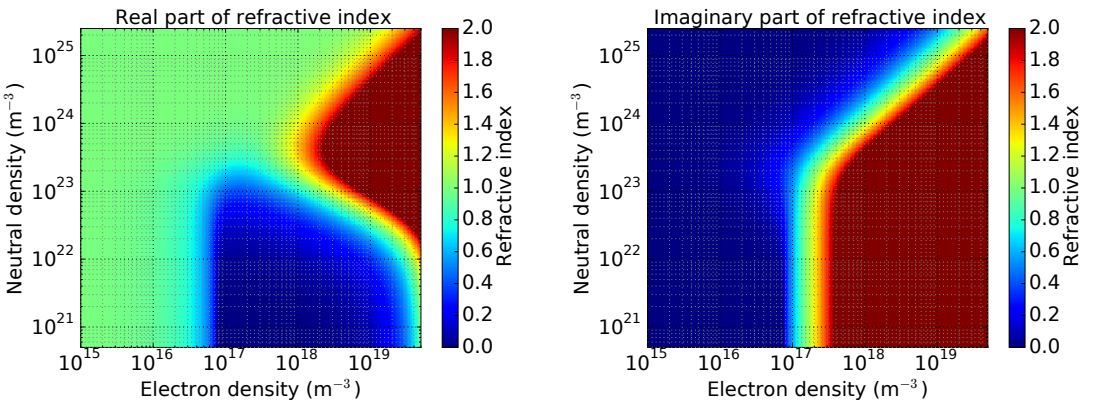

FIG. 3: The real and imaginary part of the refractive index as function of the CO_2 and electron density. The real part of the refractive index shows different behaviour below and above a neutral density of 2.3×10^{23} m^{-3} for electron densities below and above the critical electron density of 7.5×10^{16} m^{-3}.

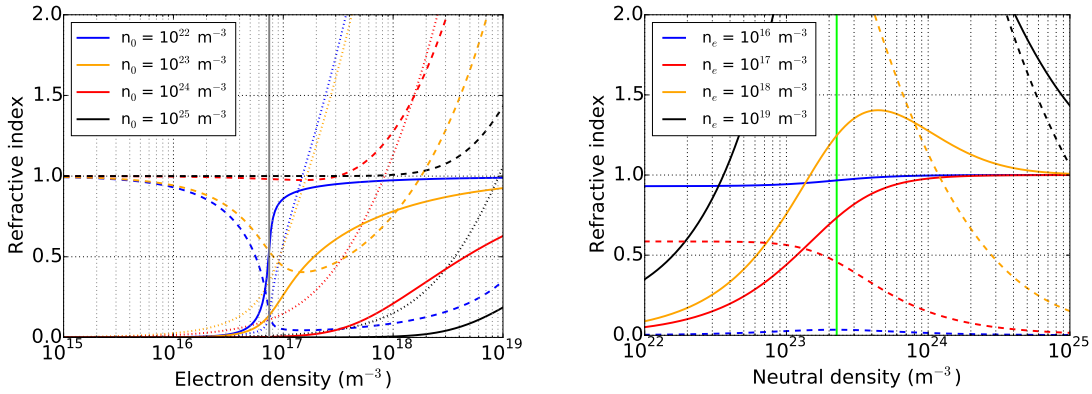

FIG. 4: Left: the real (dashed lines) and imaginary (dotted lines) part of the refractive index as function of electron density at various neutral densities. The reflection coefficient is indicated with solid lines. At low neutral densities, the reflection jumps to 1 above the critical density. When the collision frequency ν_{e-h} increases, the criteria for propagation are relaxed. Right: The real (solid lines) and imaginary (dashed lines) part of the refractive index as function of the neutral density for various electron densities. The green line marks the neutral density at which the collision frequency ν_{e-h} equals the microwave frequency ω in the absence of e-i collisions.

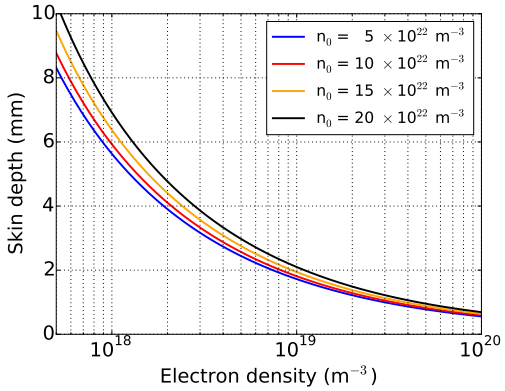

FIG. 5: Calculated skin depths as function of the electron density for various neutral densities. Using this graph the electron density can be estimated for a given neutral density with a measurement of the plasma size.

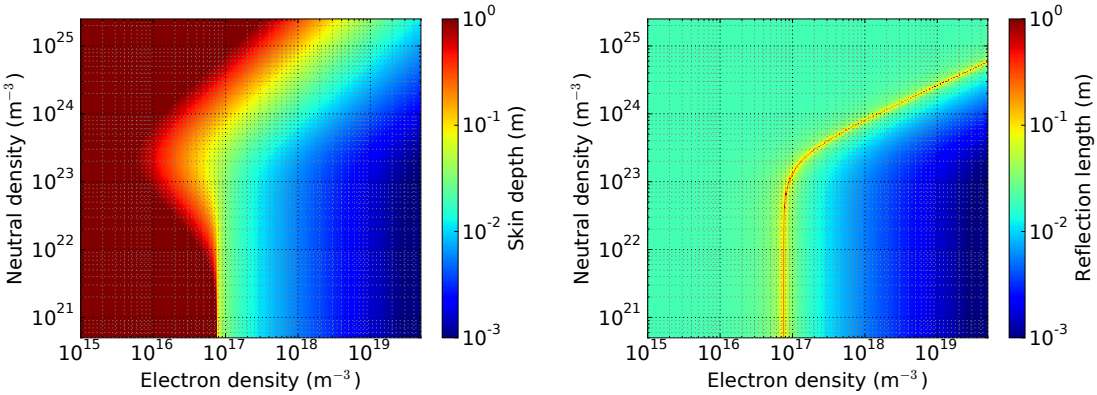

FIG. 6: Length scales of absorption and reflection as function of the electron and neutral density.

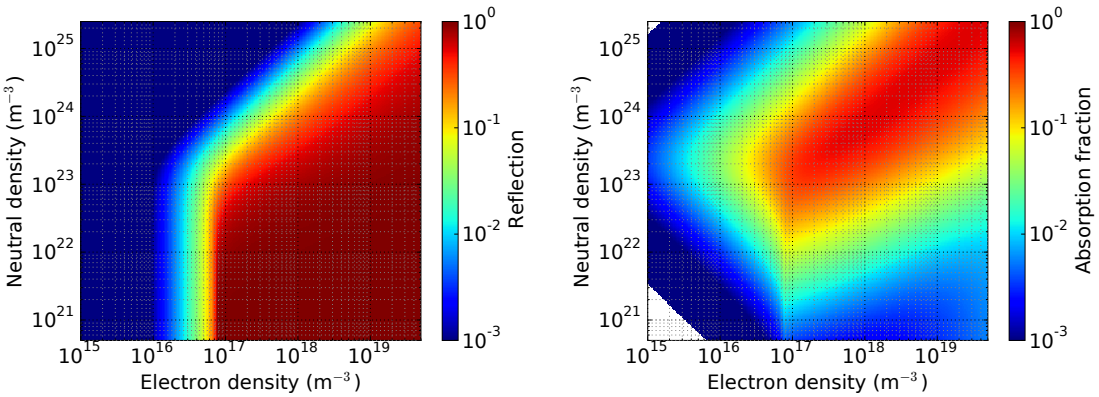

FIG. 7: Reflection coefficient (left) and absorption fraction (right) as function of the electron and neutral density for a 1D plasma of 1 cm wide.

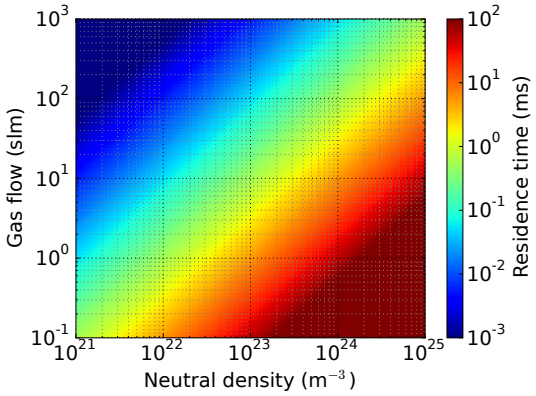

FIG. 8: Calculated residence times for a reactor with a 27 mm inner diameter quartz tube and an active volume of 43.2 mm length.

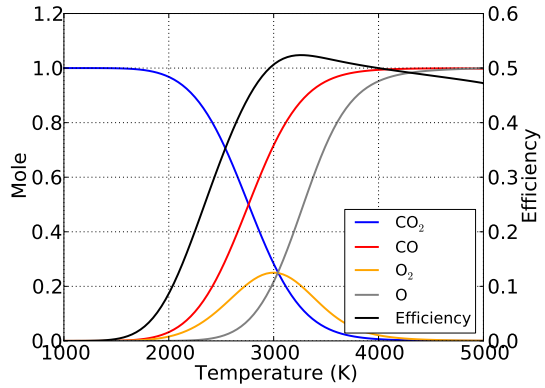

FIG. 9: The equilibrium composition of a carbon dioxide mixture as function of temperature at a pressure of 100 mbar[11,12].

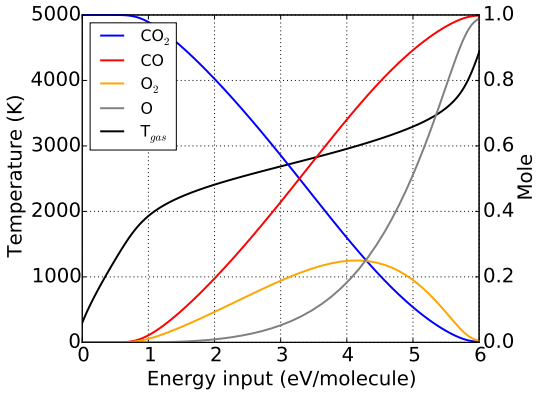

FIG. 10: Calculated gas composition and temperature as function of the specific energy input at a pressure of 100 mbar.

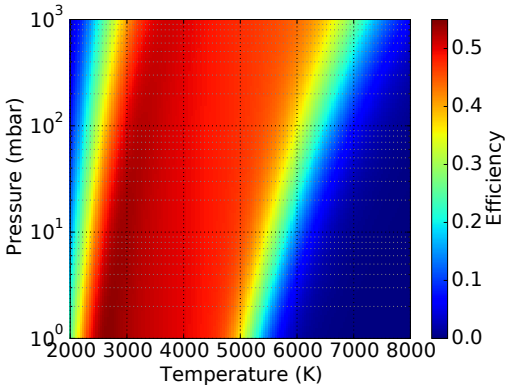

FIG. 11: The efficiency in case of ideal quenching as function of temperature and pressure. There is a large region in parameter space where efficiencies around 50 % are attainable.

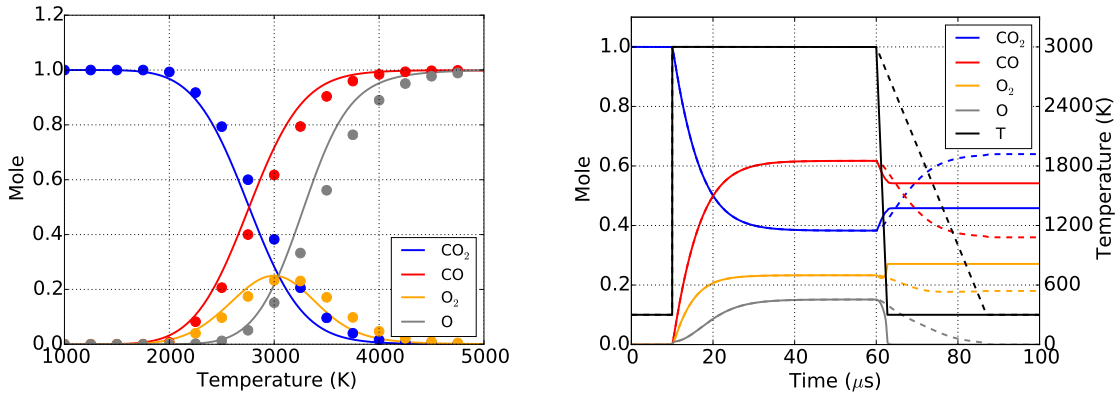

FIG. 12: Left: comparison of the CEA code (lines) and the 0-D model based on the rate coefficients (dots). The overall behaviour of the system of equations matches the CEA equilibrium calculation. Right: Two temperature evolutions with cooling rates of 10^8 and 10^9 K/s (dashed and solid lines). Two different temperature evolutions are included to illustrate that the composition changes as the CO_2 mixture heats and cools.

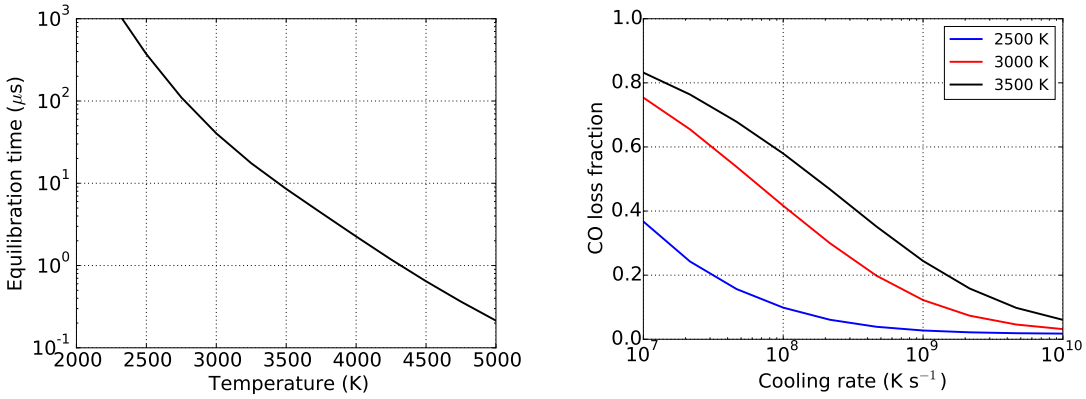

FIG. 13: Left: CO equilibration time as function of equilibrium temperature. A CO_2 mixture reaches chemical equilibrium on a microseconds timescale, thus, high cooling rates are needed to suppress CO loss. Right: CO loss fractions as a function of the cooling rate. The increasing O radical concentration with temperature leads to a larger fractional CO loss.

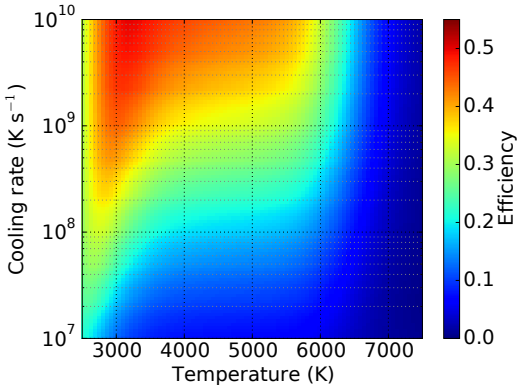

FIG. 14: The efficiency of thermal CO production in the case of linear cooling rates. Sufficiently high cooling rates on the order of 10^9 K s^{-1} inhibit back reactions, and energy efficiencies in excess of 40 % are reached.

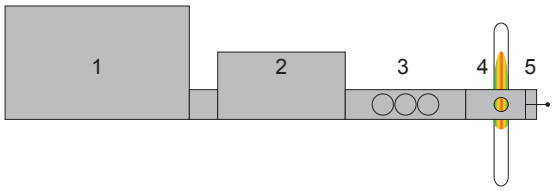

FIG. 15: The microwave setup consists of a magnetron (1) and a three port circulator with a matched, actively cooled load (2) which serves to shield the source from reflected microwaves. A sliding short (5) and a three-stub tuner (3) maximize the electric field at the location of the plasma in the quartz tube (4).

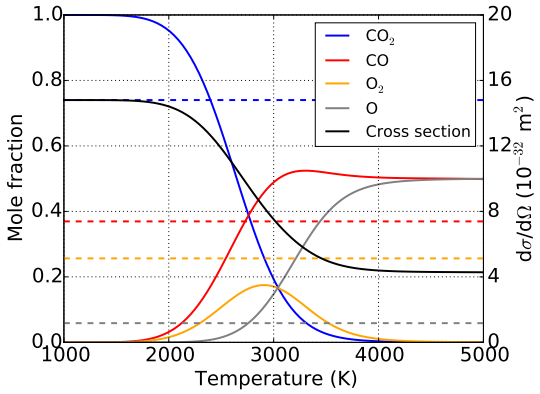

FIG. 16: The equilibrium composition is used to calculated an effective cross section. The dashed lines indicate the cross sections for individual species.

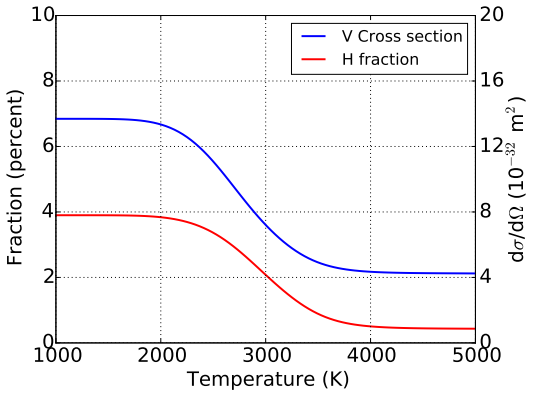

FIG. 17: The equilibrium composition is used to calculated an effective cross section for the different polarization components. The ratio of the two components changes with temperature because of the different depolarization properties of the scattering species.

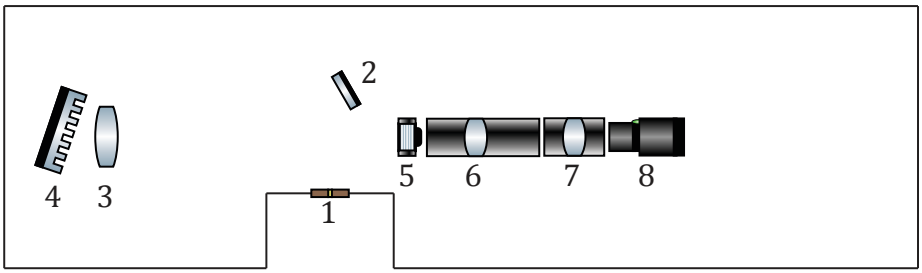

FIG. 18: A schematic of the spectrometer. Light enters via the slit (1), is reflected by a mirror (2) passes through the Littrow lens (3), refracts on the grating (4), passes the Littrow lens again, is amplified by the image intensifier (5), which is projected by lenses (6,7) onto the CCD (8).

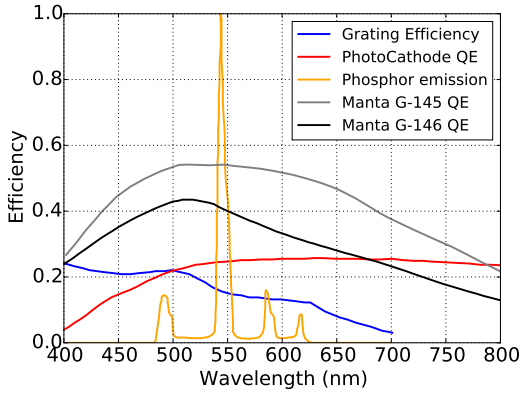

FIG. 19: Efficiencies of components in the Solar Fuels spectrometer taken from the manufacturer specifications.

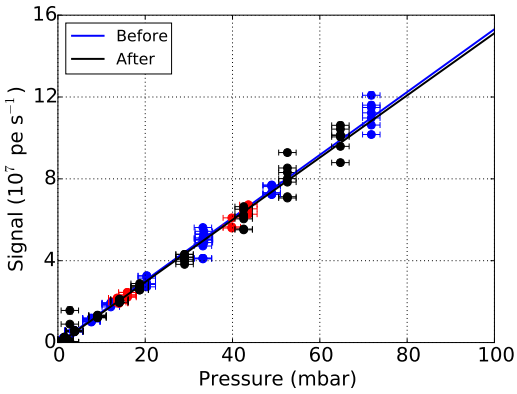

FIG. 20: Before and after experiments the signal intensity is measured as function of pressure to calibrate the sensitivity of the detection branch. Red points were measured during experiments. Similar throughputs over the course of the day indicate that the alignment of the optical system is stable. Intensity variations are used to calculate the statistical errors.

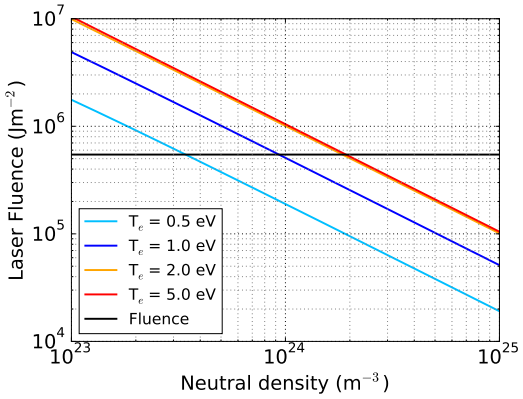

FIG. 21: Critical laser fluences for an electron heating of 10 %. An electron density of 10^{19} m^{-3} is used, but the results are not sensitive to this value since the ν_{e-h} is dominated by electron-neutral collisions. The fluence reached in the experiment is indicated in black.

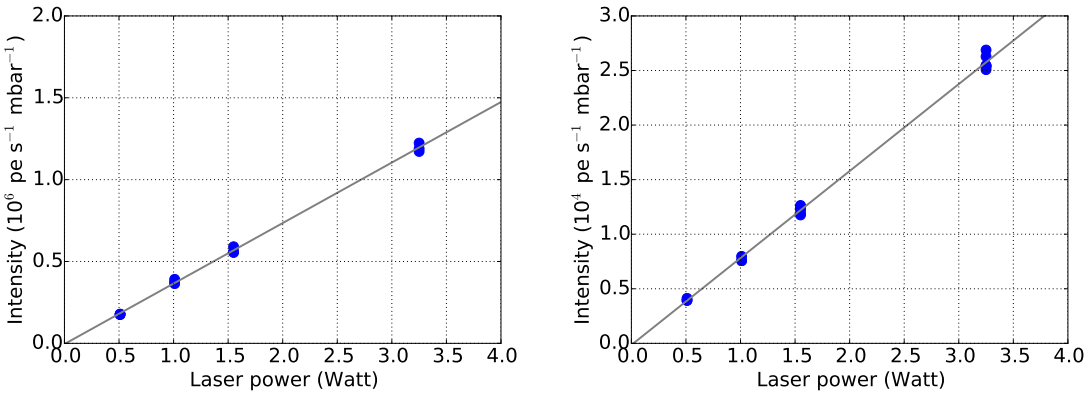

FIG. 22: Laser power scans in 120 mbar CO_2 (left) and in a 3 slm CO_2 plasma at 120 mbar and 830 Watt power input (right). To eliminate scatter, the intensities are normalized to the pressure.

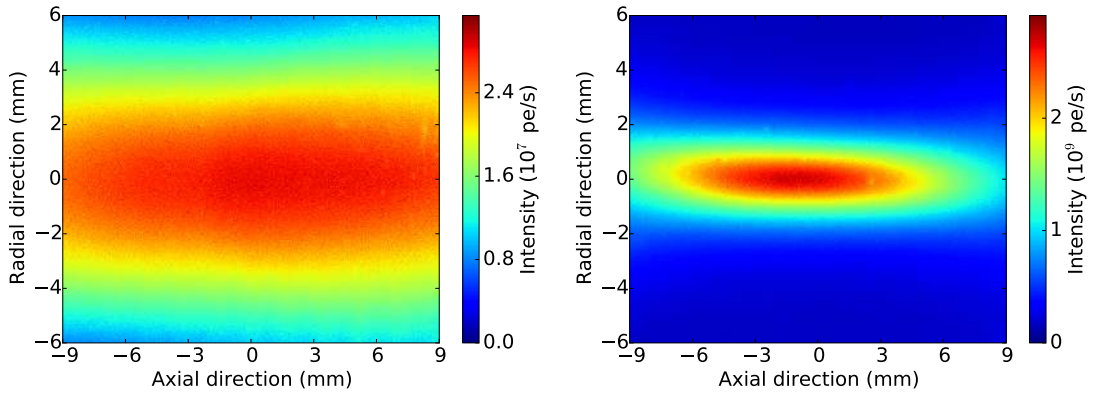

FIG. 23: Two optical emission measurements that illustrate the difference between the diffuse and contracted operating regime. Left: diffuse emission at a pressure of 42 mbar and 221 Watt input power. Right: contracted emission at a pressure of 170 mbar and 420 Watt input power.

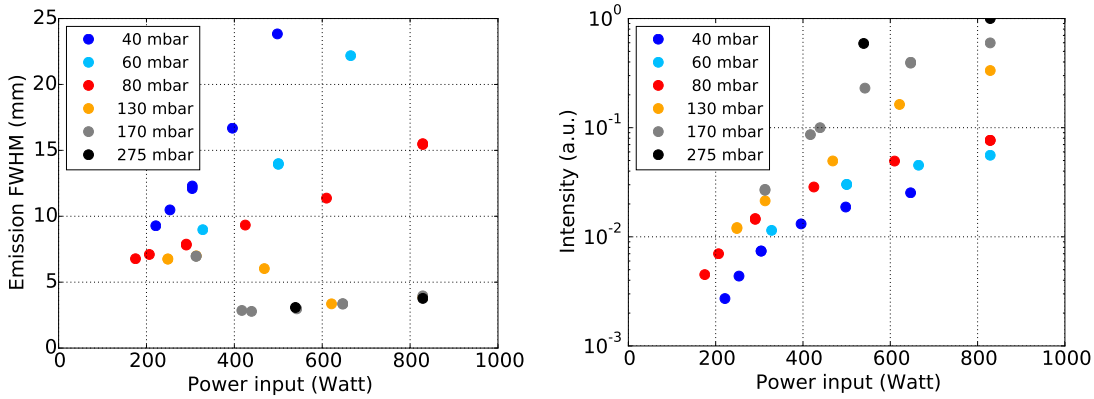

FIG. 24: The FWHM and total intensity of the optical emission of the plasma. Left: the FWHM of the radial emission profile increases with power below approximately 130 mbar. Above this pressure the plasma width constricts to a few mm, and becomes independent of the microwave power. Right: The emission intensity increases linearly with power. At higher pressures, the emission is more intense. Deviations from the trend at higher power input is due to emission outside the detection volume.

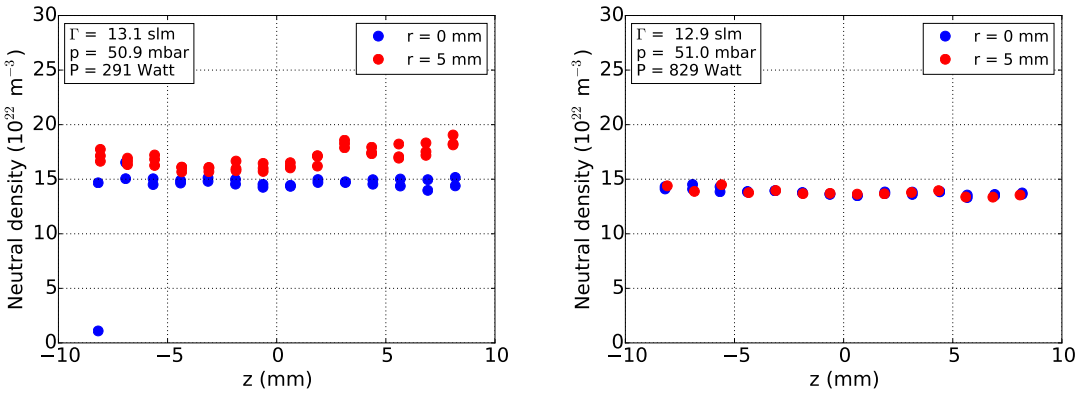

FIG. 25: Axial profiles of the neutral density measured at different radii show minor variations. In the diffuse regime, the plasma becomes radially homogeneous as the input power increases.

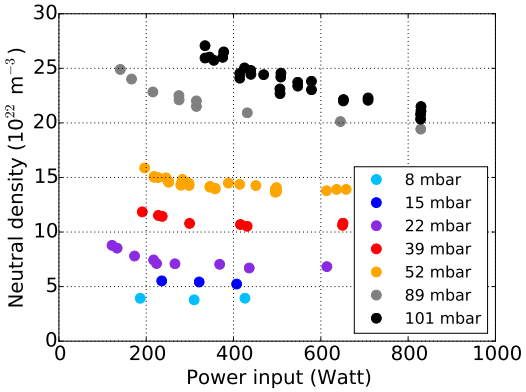

FIG. 26: The neutral density in the center of the discharge for various pressures. Different flow rates were used at pressures of 39 mbar and higher.

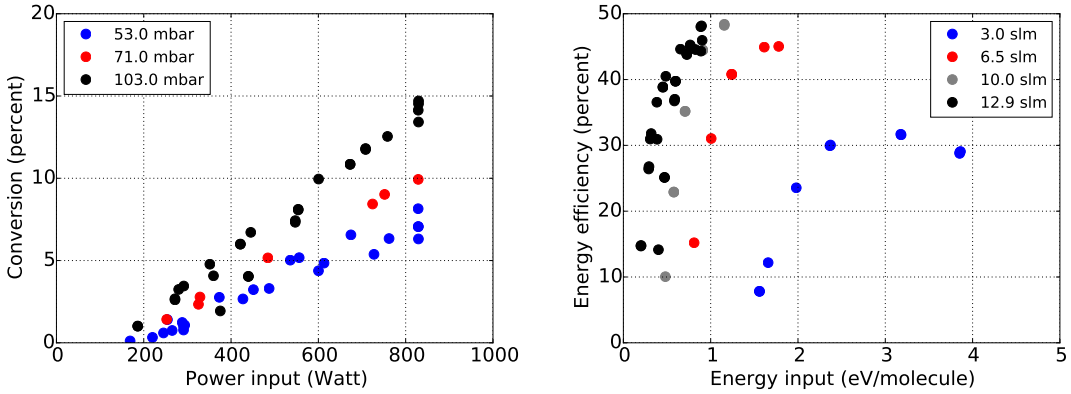

FIG. 27: Left: conversion degree as function of microwave power for various pressures at an input flow of 13 slm. Right: Energy efficiencies as function of specific energy input at a reactor pressure of 103 mbar. At low flow rates, the energy efficiency becomes lower, this is attributed to increased losses for longer residence times.

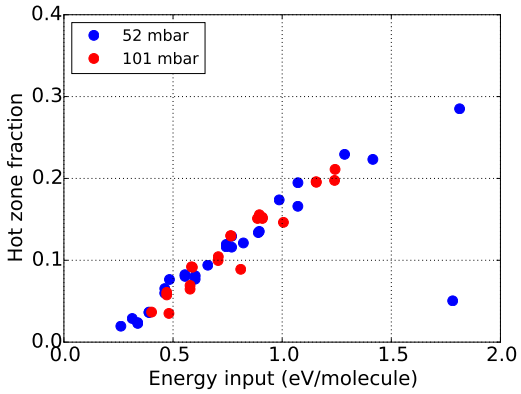

FIG. 28: Hot zone fraction as function of the specific energy input for diffuse discharges, using the two-temperature model with the measured central temperatures and conversion degrees.

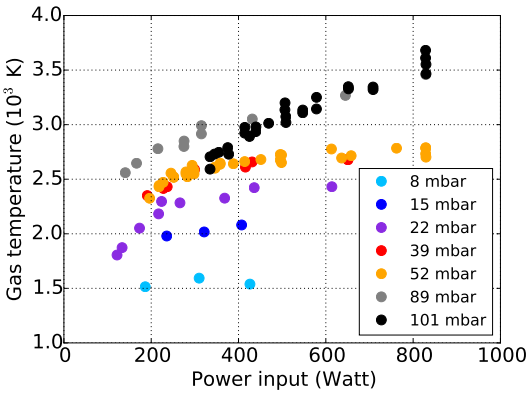

FIG. 29: The gas temperature in the center of the discharge calculated with the neutral density and reactor pressure.

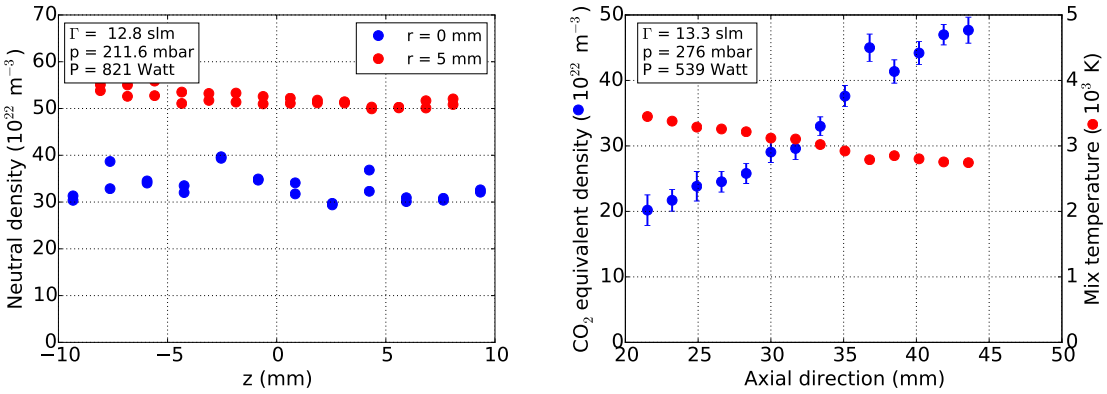

FIG. 30: Axial profiles of the neutral density in the microwave cavity and afterglow of the plasma for contracted discharges. Left: in the contracted regime, there are pronounced radial gradients in the neutral density profiles, a consequence of the peaked power deposition profile. Right: The CO_2 equivalent density increases in the afterglow, but the temperature decrease is modest as result of the temperature dependent cross section used in the analysis.

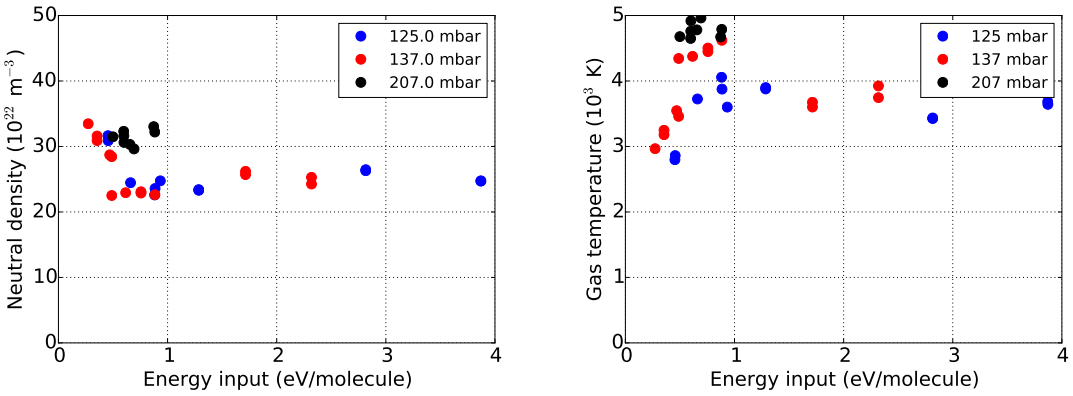

FIG. 31: On axis neutral densities (left) and temperatures (right) are interpreted assuming a thermal mixture as as calculated in Figure **??**.

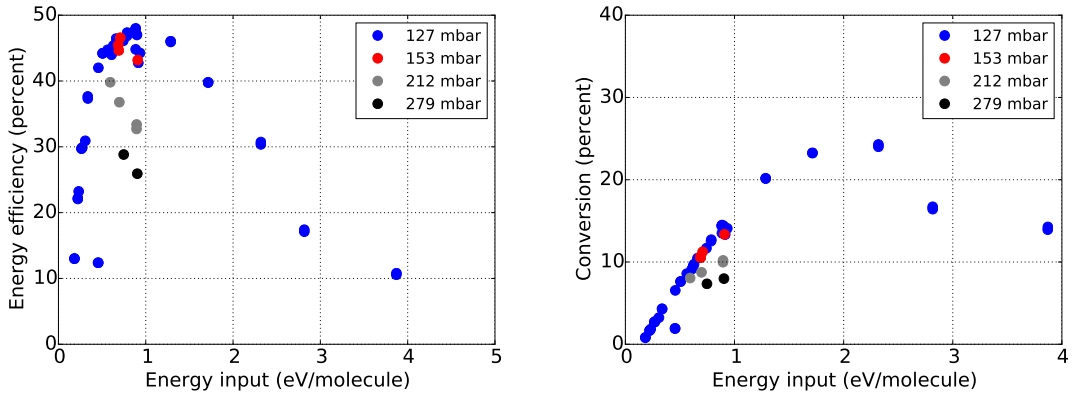

FIG. 32: The conversion degree (left) and energy efficiency (right) as a function of the specific energy input in the constricted regime.